fluids

MDPI

Article

Controlling the Chaotic Motions of an Airfoil with a Nonlinear Stiffness Using Closed-Loop Harmonic Parametric Excitation

Robert Bruce Alstrom

Department of National Center for Physical Acoustics (10001011), University of Mississippi, University, MS 38677, USA; engsci97@gmail.com

Received: 26 August 2020; Accepted: 23 September 2020; Published: 28 September 2020

Abstract: The purpose of this research is to conduct a preliminary investigation into the possibility of suppressing the flutter and post-flutter (chaotic) responses of a two-dimensional self-excited airfoil with a cubic nonlinear stiffness (in torsion) and linear viscous damping via closed-loop harmonic parametric excitation. It was found that the initial configuration of the proposed control scheme caused the torsional/pitch dynamics to act as a nonlinear energy sink; as a result, it was identified that the mechanisms of vibration suppression are the *resonance capture cascade* and the short duration or *isolated resonance capture*. It is the isolated resonance capture that is responsible for the second-order-like damping and full vibration suppression of the aeroelastic system. The unforced and closed-loop system was subjected to random excitation to simulate aerodynamic turbulence. It was found that the random excitation suppresses the phase-coherent chaotic response, and the closed-loop system is susceptible to random excitation.

Keywords: closed-loop harmonic parametric excitation; continuous-time flutter control; time–frequency analysis; wavelet spectra; transient physics; control-induced nonlinear energy sink

1. Introduction

In this paper, a self-excited two-dimensional airfoil with a cubic nonlinear stiffness in torsion is considered. It has been demonstrated that the airfoil exhibits chaotic dynamics in steady incompressible flow [1]. Ramesh and Narayanan [2] employed a control perturbation signal that consisted of an error signal with time delay multiplied by a proportional gain. They demonstrated that a simple control law could transition a chaotic aeroelastic response to stable periodic orbits. However, they could not completely suppress the limit cycle oscillation. The control law is indirectly quasi-periodic. The control perturbation signal in Ramesh and Narayanan's work is implemented by augmenting the airspeed parameter Q; this is essentially parametric excitation (PE). Generally, parametric excitation means that one or all of the coefficients (i.e., stiffness or damping coefficients) of the governing equations of the system are time-varying, but not necessarily harmonic. If the parametric excitation is harmonic, then the amplitude, frequency, and phase angle are selected such that the overall system displacements are stabilized and reduced and/or suppressed. In some works on parametric excitation, the term *quenched* may be used to describe full suppression. The following paragraphs will discuss some examples of quasi-periodic parametric excitation and direct harmonic periodic excitation as a means of vibration control.

Tondl, Ecker, Dohnal, and their respective colleagues have presented work on a variety of parametrically excited mechanical systems [3–6]. In all these studies, the mass/inertia, stiffness, and damping have a harmonic formulation based on the Mathieu equation. Each of these works has resulted in similar conclusions on the topic of parametric excitation as a means of vibration control

and can be summarized as follows: (a) Suppression is achieved when the frequency of excitation is near the antiresonant frequency or the difference of the two primary frequencies; (b) amplification occurs when the frequency of excitation is near a parametric resonance or the sum of the primary frequencies; (c) vibration suppression can also be achieved when the parametric forcing amplitude undergoes a bifurcation.

Chin et al. [7] derived parametrically excited equations of motion for a simply supported panel in supersonic flow in order to obtain equilibrium solutions and stability of the plate. The analysis identified that flutter suppression was obtained in the vicinity of a combination parametric resonance. It should be noted here that a simply supported panel has been shown to respond like a Duffing oscillator. Poirel and Price [8] present work on an airfoil with a hardening cubic structural nonlinearity subjected to longitudinal turbulence. They present conclusions for a case where the flutter speed is advanced by the presence of a random gust while the Hopf bifurcation is postponed; this lowered the dynamic pressure associated with the mean airspeed for which flutter occurs, and its effect is parametric as it acts via the airspeed.

Ibrahim and Castervete [9] present research on the flutter suppression of a flexible plate wing using parametric excitation. Specifically, the wing is modeled as a plate-like beam and is subjected to harmonic base excitation in the plane of the largest rigidity. The nonlinear coupling arises from the displacement of the elastic axis. The method of multiple scales was used to obtain the nonlinear response at the critical flutter speed and a subcritical flow speed. The calculated domains of attraction and bifurcation diagrams revealed conditions under which the amplitude of parametric excitation, Y_0, provides a stabilizing effect. The basins of attraction for different values of excitation amplitude show that stabilization takes place above a critical excitation level. Below the critical excitation amplitude, the aeroelastic systems undergo limit cycle oscillations, a cascade of period doubling and chaos. For an airspeed slightly above the critical flutter speed, the system exhibits a spike train. The spike train is a phenomenon also seen in neurological activity and surface pressure fluctuations in the reverse flow region of a wing with separated flow. These spike train dynamics preceded a stable aeroelastic response; here, stable means a limit cycle oscillation (LCO). In this study, the critical parameter was not the parametric excitation frequency, but the excitation amplitude. The examples presented here are not exhaustive. From the few examples presented here, one can conclude that the variation in parametric excitation frequency, amplitude, and if necessary, phase angle results in the open-loop stabilization of both mechanical and aeromechanical systems. Discrete variation in the primary parameters mentioned above only provide suppression at those predetermined values and over a finite bandwidth, which may not be appropriate for the more operational applications.

For aeromechanical systems that have an operational role such as wings and helicopter rotor systems, the operating conditions do not remain constant; thus, closed-loop control is required. Two examples of experimental vibration suppression control via parametric excitation are presented in the following paragraphs. Harold [10] presents work on a device called the Smart Spring. The Smart-Spring was developed at Carleton University and the Canadian National Research Council (CNRC). The Smart Spring concept is a semi-active approach to vibration suppression that utilizes an actively tunable impedance device. The Smart Spring possesses a large bandwidth and can generate large control forces at relatively low power; this is characteristic of an active tunable vibration absorber (ATVA). The large bandwidth is made possible because of the adaptive variable impedance of piezoceramic actuators; these actuators are able to vary the stiffness, damping, and mass-coupling of the Smart-Spring. Numerical results for the base-excited version of the Smart Spring coupled with a state-switched controller [11] showed that the device could successfully suppress the system displacements induced by external excitation.

The torsional version of the Smart Spring was used for blade root impedance control for a wind tunnel experiment involving a single helicopter rotor blade. The torsional variable impedance device was installed at the root of the rotor blade and an adaptive notch filter based on the well-known filtered least-mean-square (LMS) filter was developed for closed-loop control. The blade assembly

is placed behind a square tube vortex generator for external excitation. The results demonstrated (via displacement time series) that once the control law and Smart Spring were engaged, the amplitude of oscillation and reaction load at the blade root were significantly reduced [12,13].

Athalye [14] completed dissertation work on notch filter feedback control of a forced Duffing oscillator in the chaotic regime. Athalye was able to demonstrate that the notch filter feedback can eliminate the chaotic dynamics for a given set of fixed filter parameters. More specifically, the notch filter feedback transitioned the chaotic Duffing oscillator to a stable limit cycle oscillation. Ahlborn and Parlitz [15] present both numerical and experimental results on the application of notch filter feedback applied to the self-excited Rossler system and a laser. A notch filter can be tuned such that particular frequencies can be removed from the system. In fact, they demonstrated that using two notch filters can transition the chaotic Rossler system to full suppression; this was achieved by selecting frequencies that are responsible for the chaotic dynamics in the first place, namely the fundamental frequency and the first superharmonic in the case of the Rossler system. Notch filter feedback drives the dynamical system toward a stable fixed point. The summation of output signals from a bank of notch filters (in parallel) form a nonstationary multifrequency perturbation signal that would have a stabilizing effect on a dynamical system.

The purpose of this research is to conduct a limited preliminary investigation into the possibility of suppressing flutter and the post-flutter (chaotic) response of the given two-dimensional aeroelastic Duffing oscillator via closed-loop harmonic parametric excitation and to understand the mechanisms behind the vibration suppression, if any. The paper is organized as follows: Section 2 provides a full description of the mathematical modeling and control implementation; Section 3 discusses the signal processing methods to be used in this work, followed by Section 4 in which the results and discussion are presented. Section 5 presents conclusions, and future research directions are given in Section 6.

2. Mathematical Modeling and Control Implementation

Figure 1 shows a schematic of an airfoil with the following parameters: $\mu = 20$, $a = -0.1$, $b = 1$ m, $x_\alpha = 0.25$, $r_\alpha^2 = 0.5$, $(\omega_h/\omega_\alpha)^2 = 0.2$, $\omega_h = 28.1$ Hz, and $\omega_\alpha = 62.8$ Hz, where $\mu = m/\left(\pi\rho b^2\right)$, ρ is the air density, m is the mass, b is the semichord point, ab is the distance of the elastic axis E from the midchord point, $(0.5 + a)b$ is the distance of E from the aerodynamic focus F, $x_\alpha b$ is the distance of the center of gravity from E, $r_\alpha b$ is the radius of gyration of the airfoil with respect to E, and ω_h and ω_α are the eigenfrequencies of the constrained two-degree-of-freedom system associated with the linear plunging and the pitching springs, respectively.

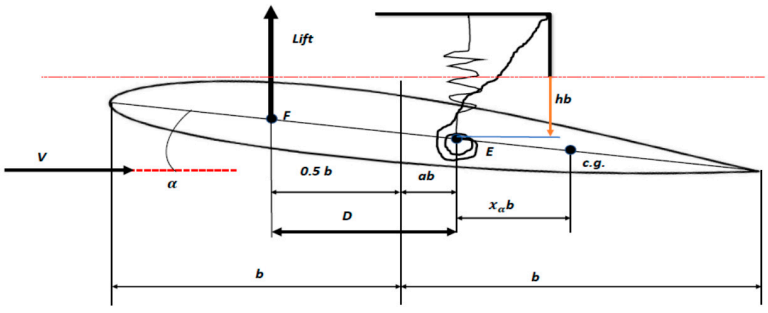

Figure 1. Sketch of two-dimensional airfoil.

The equations of motion are given as follows:

$$\mu\ddot{h} + \mu x_\alpha\ddot{\alpha} + \mu(\omega_h/\omega_\alpha)^2 h = -2Q\alpha\mu x_\alpha\ddot{h} + \mu r_\alpha^2\ddot{\alpha} + \mu r_\alpha^2\alpha = (1 + 2a)Q\alpha \tag{1}$$

where h is the plunging or bending displacement divided by b, α is the pitching angle, the airspeed parameter $Q = (V/b\omega_\alpha)^2$, and V is the airspeed. The terms plunge or bending will be used interchangeably throughout the paper. The time, t, in Equation (1) is $t = \omega_\alpha\tau$, where t is the

nondimensional time and τ is the real time in seconds. By introducing the viscous terms and a cubic torsional stiffness, the equations of motion can be rewritten as Equation (2).

$$\ddot{h} + 0.25\ddot{\alpha} + 0.1\dot{h} + 0.2h + 0.1Q\alpha = 00.25\ddot{h} + 0.5\ddot{\alpha} + 0.1\dot{\alpha} + 0.5\alpha + e\alpha^3 - dQ\alpha = 0 \quad (2)$$

where e is the nonlinear stiffness factor and $d = 2D/\mu b$. Subsequent calculations are performed at e = 20 and d = 0.08, and the initial conditions are $\left(h_0,\ \dot{h}_0, \alpha_0, \dot{\alpha}_0\right)$ = (0,0,0.01,0). The addition of the cubic nonlinearity makes the aeroelastic system a 2 degree of freedom Duffing oscillator. The simulation is carried out in the MATLAB/SIMULINK environment and the equations are solved using a fourth-order Runge Kutta solver sampled at 100 Hz. The system frequencies or frequency ratios are of the form $(\omega/\omega_\alpha)^2$; thus, if one wishes to extract the actual frequency in Hz, they can do so by using the squared frequency ratio. Note that ω is the angular response frequency. Zhao and Yang performed a parametric analysis for the airspeed parameter Q and the parameter d. The results of this analysis are summarized in Figure 2. Note the region called the chaotic pockets zone and the Hopf bifurcation boundary. For a detailed discussion of the parameter plane shown below, the reader is directed to Zhao and Yang's work [1]. The uncontrolled phase plots depicting the chaotic dynamics in the pitch and plunge degrees of freedom are shown below in Figure 3. A table with natural and parametric resonance frequency ratios is provided for reference (see Table 1).

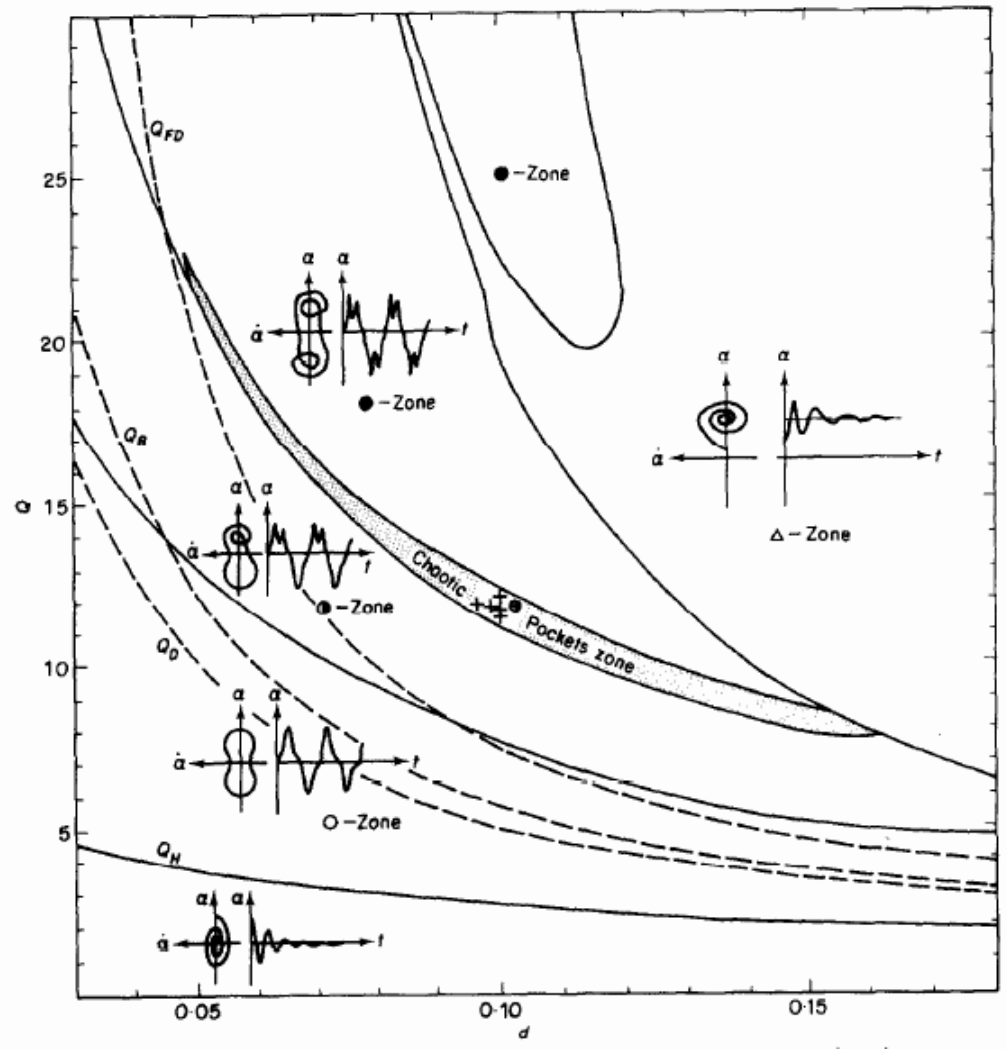

Figure 2. (Q, d) parameter plane with boundaries for different types of motion [1].

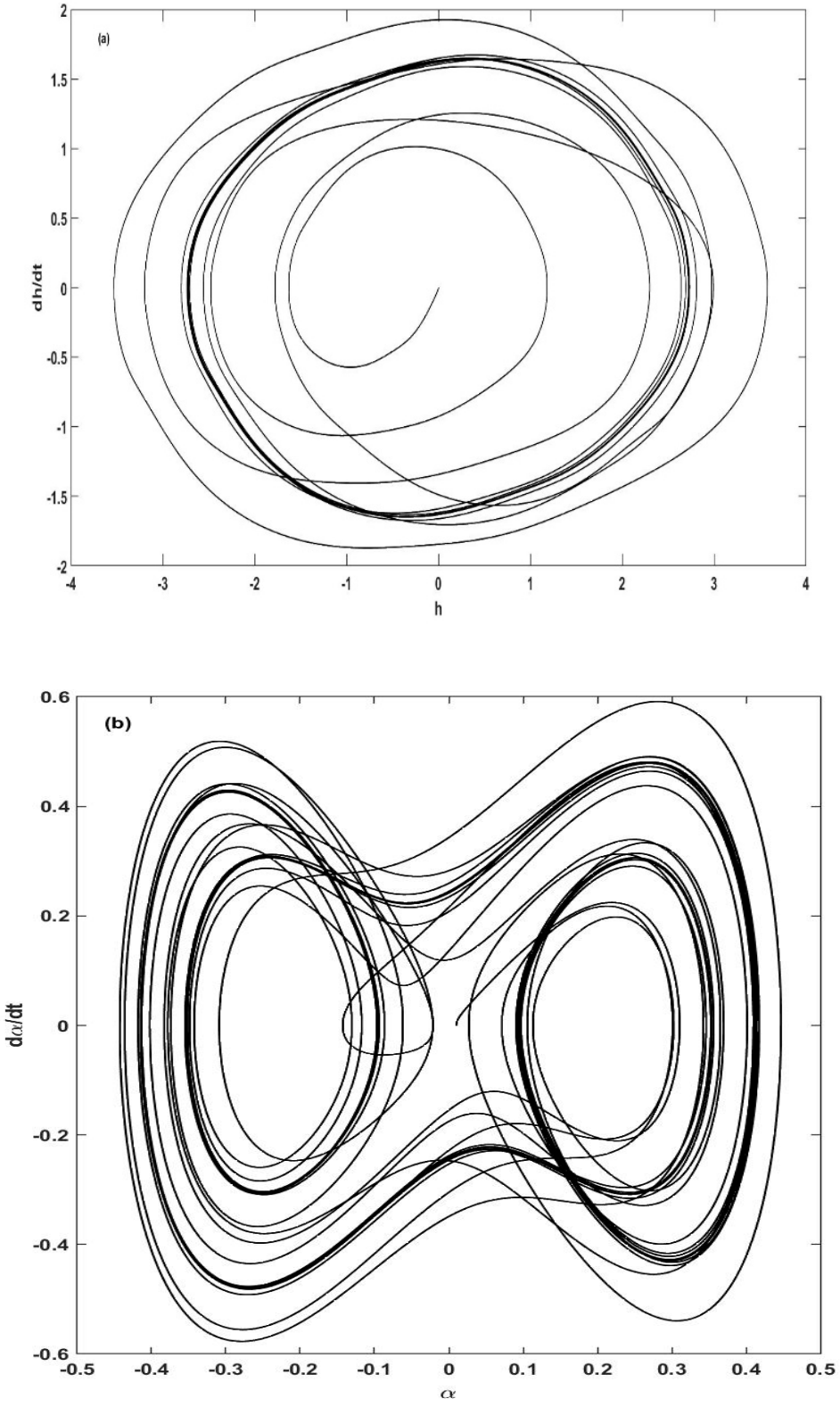

Figure 3. Phase plot depicting the chaotic motion of airfoil (Q = 15.6, e = 20, d = 0.08). (**a**) Phase plot of the bending (h) dof. (**b**) Phase plot of the pitch (α) dof.

Table 1. Natural and parametric resonance frequencies.

Natural Frequencies (Hz)	**Frequency Ratio**
$\omega_h = 28.1$ $\omega_\alpha = 62.8$	$\left(\frac{\omega_h}{\omega_\alpha}\right)^2 = 0.2$
Parametric Resonance Frequencies (Hz)	**Frequency Ratio**
$2\omega_h = 56.2$	$\left(\frac{2\omega_h}{\omega_\alpha}\right)^2 = 0.8$
$2\omega_h/2 = 28.1$	$\left(\frac{\omega_h}{\omega_\alpha}\right)^2 = 0.2$
$\omega_h + \omega_\alpha = 90.9$	$\left(\frac{\omega_h+\omega_\alpha}{\omega_\alpha}\right)^2 = 2.0951$
$(\omega_h + \omega_\alpha)/2 = 45.45$	$\left(\frac{\omega_h+\omega_\alpha}{2\omega_\alpha}\right)^2 = 0.5238$
$2\omega_\alpha/3 = 41.866$	$\left(\frac{2\omega_\alpha}{3\omega_\alpha}\right)^2 = 0.4444$
Parametric Antiresonance Frequencies (Hz)	**Frequency Ratio**
$\omega_\alpha - \omega_h = 34.7$	$\left(\frac{\omega_\alpha-\omega_h}{\omega_\alpha}\right)^2 = 0.3053$
$(\omega_\alpha - \omega_h)/2 = 17.35$	$\left(\frac{\omega_\alpha-\omega_h}{2\omega_\alpha}\right)^2 = 0.0763$

The control signal (Equation (3)) is a linear combination of harmonic terms, the sum of which is multiplied by the airspeed parameter Q_0.

$$Q_e = Q_o F(t),\ F(t) = \sum_{i=1}^{4} w_i f_i(t)\ and\ f_i(t) = \sin(x_i t)\ or\ \cos(x_i t) \tag{3}$$

The torsional and bending displacements and their respective velocities (four states) are used in the arguments of the harmonic terms; the harmonic terms are bounded and the feedback signals track the time-continuous changes in amplitude and frequency, which is called self-controlling feedback [16]. The weight w is used to turn the feedback signals on (w = 1) or off (w = 0) as needed. It is important to note that not all signals or combinations of signals will yield a stable closed-loop response; therefore, the stability of the closed-loop system must be checked in and around the Hopf bifurcation boundary and in the chaotic region as identified in the (Q, d) parameter space (Figure 2). The combination of signals will not necessarily follow the presentation in the schematic, as certain combinations might have better performance. The general schematic for closed-loop harmonic parametric excitation is given below in Figure 4.

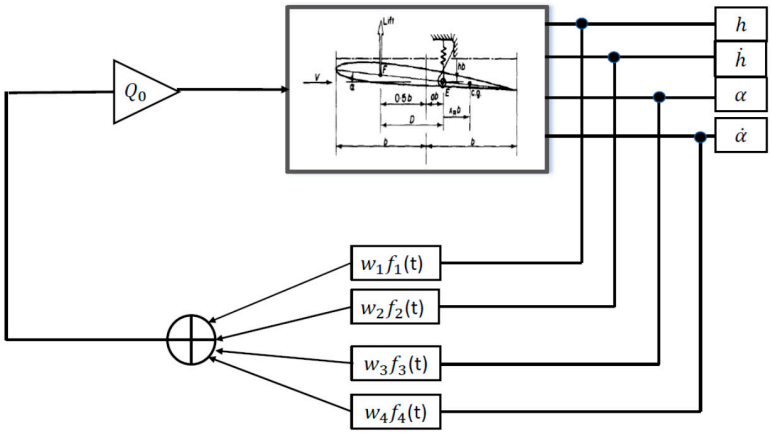

Figure 4. Schematic of closed-loop harmonic parametric excitation.

It has been demonstrated in previous research (see Section 1) that full vibration suppression using parametric excitation is achieved at discrete frequencies (parametric resonance and anti-resonance frequencies specifically).

3. Nonstationary Signal Analysis

Nonstationary signal processing is used in this study because it exposes the transient physics of the system. Spectral attenuation occurs because of synchronization and is best captured by the nonstationary signal processing methods. Its application in this instance is particularly appropriate for nonlinear systems. Specific to this study, the aeroelastic system contains a nonlinear torsional stiffness, and secondly, the control method generates a time-varying control signal [17]. Wavelet-based time–frequency analysis along with benchmark frequency ratios (see Table 1) will enable the identification and examination of the underlying nonstationary dynamics with and without closed-loop control. Time–frequency analysis is achieved by projecting the signal onto the time–frequency plane, which enables one to study the properties of the signal in time and frequency at the same time. These projections are called time–frequency representations (TFRs). The analysis in this paper utilizes both the wavelet and Hilbert transforms. The continuous wavelet transform has logarithmic frequency resolution. The wavelet transform of a function $s(t)$ is defined as:

$$W(\xi,\tau) = \int_{-\infty}^{+\infty} s(t)\psi^*_{\xi,\tau}(t)dt \tag{4}$$

where ξ and τ are scale and time variables, respectively; $\psi^*_{\xi,\tau}(t)$ represents the wavelet family generated by continuous translations and dilations of the mother wavelet. The translations and dilations are obtained by:

$$\psi_{\xi,\tau} = \frac{1}{\sqrt{\xi}}\psi\left(\frac{t-\tau}{\xi}\right) \tag{5}$$

The wavelet to be used for this analysis is the log-normal wavelet. It is defined as follows:

$$\psi(t) = e^{-\frac{2\pi f_0 \log t}{2}} \tag{6}$$

The resulting output is a time–frequency map, which is a three-dimensional plot. The z-axis is the magnitude of the wavelet transform coefficients, which indicate the amount of energy at a given time and frequency ratio. A wavelet transform spectrum is also calculated to aid in the analysis of the transient dynamics. The Hilbert transform provides the definition of a time-varying envelope function. The transform is the harmonic conjugate of the original signal. The Hilbert transform is defined as:

$$\widetilde{s}(t) = \frac{1}{\pi}\int_{-\infty}^{\infty} \frac{s(\tau)}{t-\tau}d\tau \tag{7}$$

The signal can then be represented as a complex valued function given by the conjugate harmonic pair:

$$S(t) = s(t) + i\widetilde{s}(t) \Longrightarrow A(t)e^{i\theta(t)} \tag{8}$$

where $A(t)$ is the instantaneous envelope amplitude and $\theta(t)$ is the instantaneous phase of the signal. The instantaneous frequency is the first derivative of the signal phase $\theta(t)$. If one assumes that the signal is an exponentially decaying sinusoid, then the envelope amplitude can be written as follows:

$$A(t)e^{\zeta(t)\omega(t)t} \tag{9}$$

Next, an approximation is made where the damping ratio and frequency are approximately constant. This is not valid in the strictest sense for the Hilbert transformation when the signal is not periodic or infinitely long. However, this approximation allows the system damping to be estimated

by taking the natural logarithm of Equation (9). It should be noted here that relevant spectral peaks will be tagged and different color schemes will be applied in the time–frequency maps to aid in the identification of relevant spectral features that are present after each calculation concludes. As a demonstration of the nonstationary signal processing method, the time–frequency analysis for the uncontrolled dynamics is presented in Figures 5 and 6. For the pitch displacement, it is observed that the wavelet coefficient spectra are broadband, and decrease in magnitude with increasing frequency ratio. The strongest of these peaks is located at a frequency ratio of ~0.09259 (closest to parametric antiresonance frequency ratio of 0.0763). The remaining peaks are all in the vicinity of the known parametric resonant frequency ratios. The two strongest peaks are a parametric antiresonant mode (~0.09259) and a parametric resonant mode (~0.2803). The plunge displacement vibrates at the parametric antiresonant mode of ~0.09259.

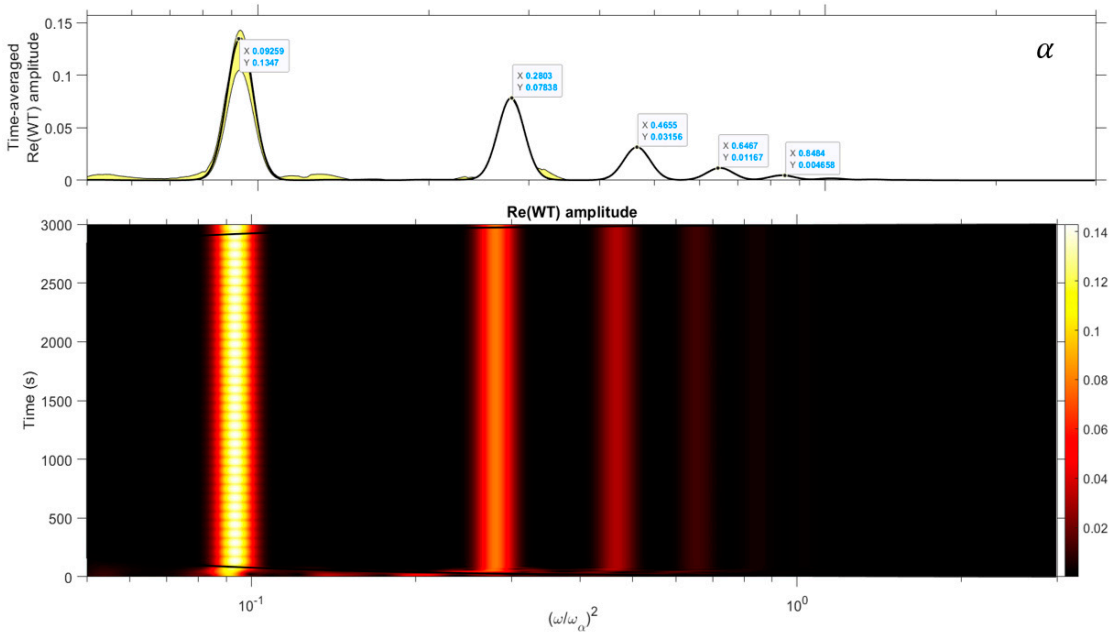

Figure 5. Time–frequency analysis of the pitch displacement.

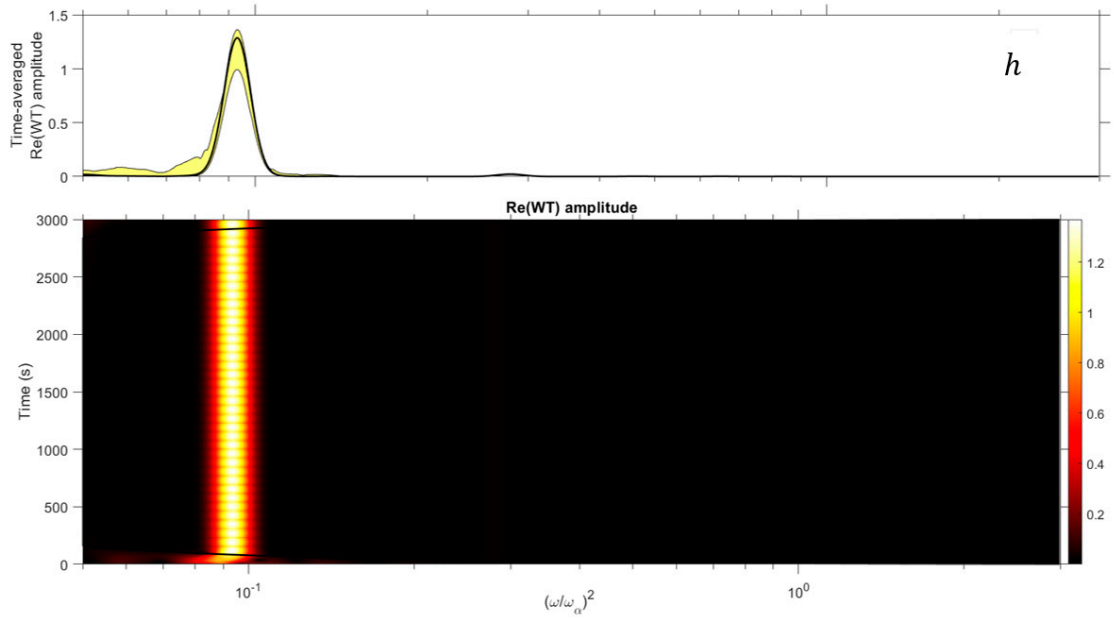

Figure 6. Time–frequency analysis of the plunge/bending displacement signal.

4. Results and Discussion

Case I: $Q_e = Q_o\left[\cos(\dot{\alpha}t)\right]$

In order to better understand the results presented in this section, we must turn to the works of the UIUC Linear and Nonlinear Dynamics and Vibrations Laboratory, specifically their work on nonlinear energy sinks (NESs). Vakakis et al. [18,19] presented a study of isolated resonance captures and resonance capture cascades. The dynamical system under study in this work is a system of damped coupled oscillators, specifically a main linear system that is fixed to a nonlinear attachment that acts like a nonlinear energy sink (NES). They demonstrated that the NES is capable of absorbing significant portions of the energies generated by transient broadband external excitations. The mechanisms of vibration suppression are by way of two mechanisms, which are the *isolated resonance capture* and the *resonance capture cascade*. An isolated resonance capture involves a single frequency about which no nonlinear energy absorption takes place between the system degrees of freedom; this type of resonance capture is typically short-lived in time and is related to a damped oscillation. The resonance capture cascade mechanism (also referred to as multifrequency vibration absorption) can be accomplished with a single NES. The resonance capture cascade mechanism is triggered when the NES vibrates at some frequency, and when enough energy has been dissipated at that frequency, the NES will 'jump' to the next frequency, dissipating the energy at the new frequency. The NES will continue to jump until all the modes have had their vibrational energy dissipated, hence the usage of the term cascade. The jump phenomena can also be interpreted as an energy-related bifurcation [20]. The aeroelastic system (see Equation (2)) in this current study can be thought of as a linear system with a nonlinear attachment; specifically, the bending degree of freedom is the *linear system* and the pitch degree of freedom is the *nonlinear attachment* with the necessary nonlinearity. The prescribed perturbation signal via parametric excitation causes the torsional nonlinear dynamics to act like a nonlinear energy sink. The control action is engaged at $t = 0$ at $Q_o = 9$ for the prescribed perturbation signal given above. Preliminary simulations with the control perturbation signal of the form $Q_e = Q_o\left[\cos(\dot{\alpha}t)\right]$ revealed that it does not suppress the limit cycle oscillations until $Q_o \sim 9$. When the airspeed parameter is less than 9, the wing oscillates (in both degrees of freedom) about a parametric antiresonant condition of ~0.08934 (which is closest to 0.0763 from Table 1). At $Q_o = 9$, we start to see the appearance of other frequency ratios as Q_o gets closer to the chaotic region. One possible reason for this is the fact that in the chaotic region, there are more unstable periodic orbits (UPOs) available for synchronization; the appearance of these other modes is primarily a function of the airspeed parameter. Figure 7 shows the time histories of the aeroelastic displacements for $Q_o = 9$. Between t = 0 and 2000, the wing exhibits a limit cycle oscillation at a frequency ratio of ~0.09. Although there is no nonlinear energy absorption during this time interval, the jump or escape from the parametric antiresonance occurs because there is energy dissipation present. Between t = 2000 and 3500 (indicated by the red lines), the system appears to 'hunt' for the next mode to lock into; at t = 3500, the system is again resonance-captured at a frequency ratio of ~0.2076, only this time, there is energy absorption. The time between resonance captures decreases with the increase in the airspeed parameter. The energy absorption is indicated by the reduction in the amplitude of the bending displacement signal for $t > 3500$. Note that there is no reduction in the pitch amplitude, but the time series becomes more visually dense, indicating a change in the frequency of oscillation. Additional visual confirmation of nonlinear energy absorption is provided by an inspection of the time–frequency analysis for the aeroelastic displacements (Figures 8 and 9). For the bending displacement (Figure 8, $t > 3500$), the reader will note that for the line of constant frequency (see white line marker in Figure 8), the corresponding wavelet transform coefficients are nearly zero as compared to the pitch displacement for the same time interval (Figure 9, $t > 3500$) where the wavelet transform coefficients are at a maximum. A resonance capture with energy absorption presents as an increase in spectral power in one degree of freedom, while the other shows a significant decrease. This decrease in spectral power corresponds to a reduction in displacement amplitude in the time domain.

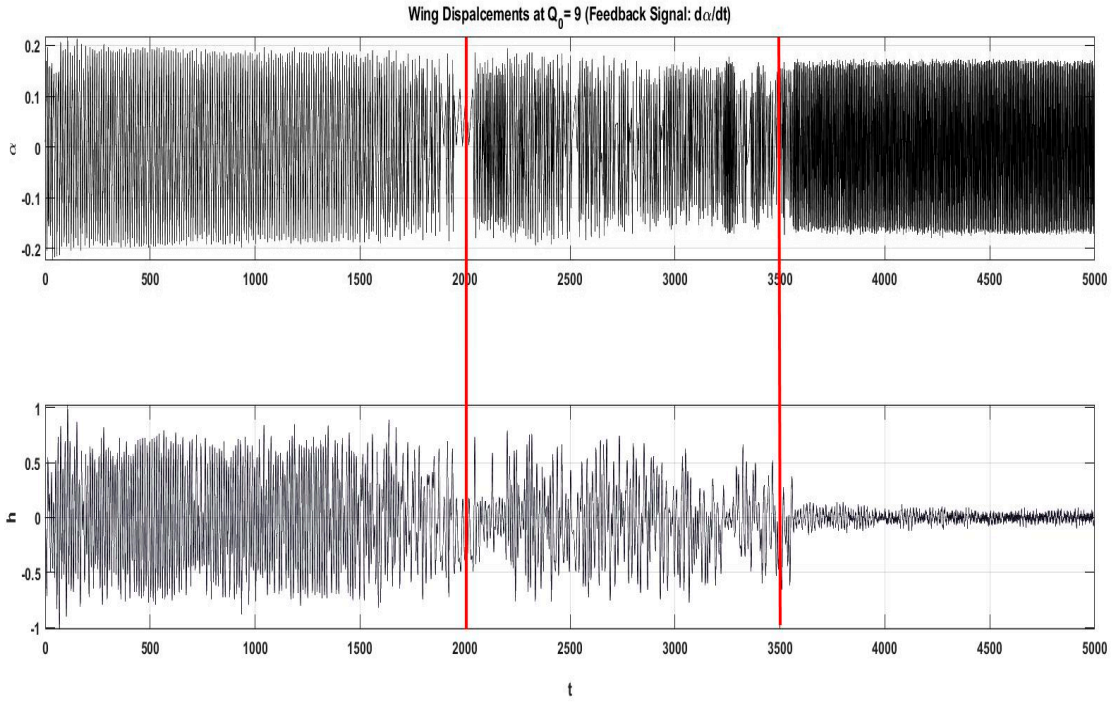

Figure 7. Wing displacements at $Q_o = 9$.

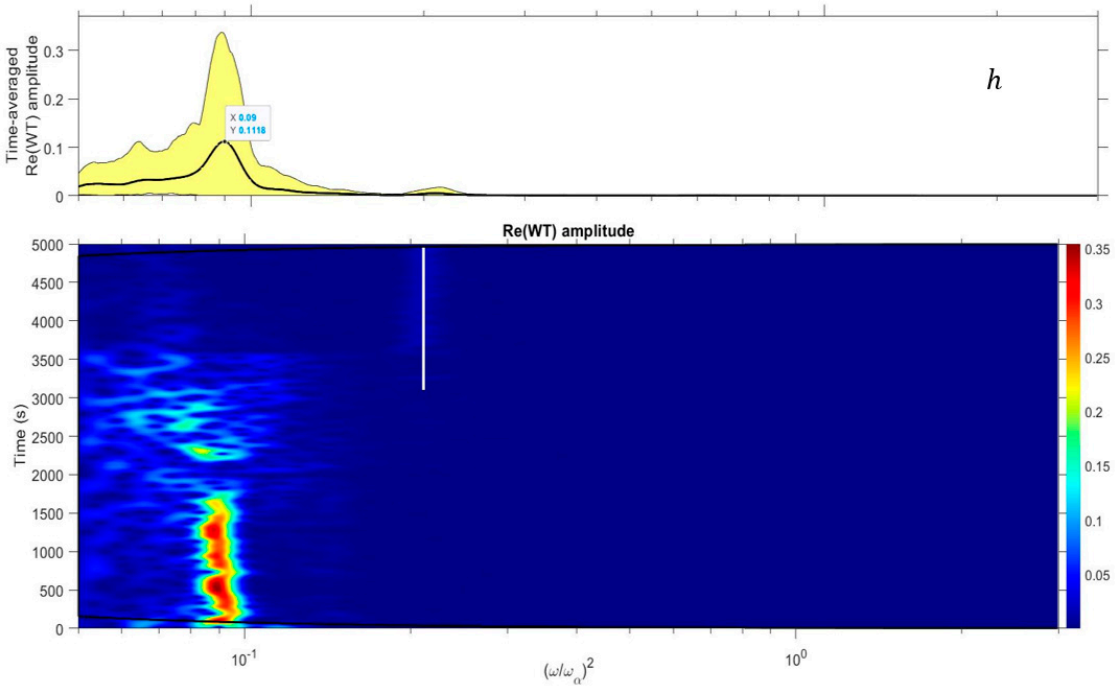

Figure 8. Time–frequency analysis of plunge/bending displacement signal ($Q_o = 9$).

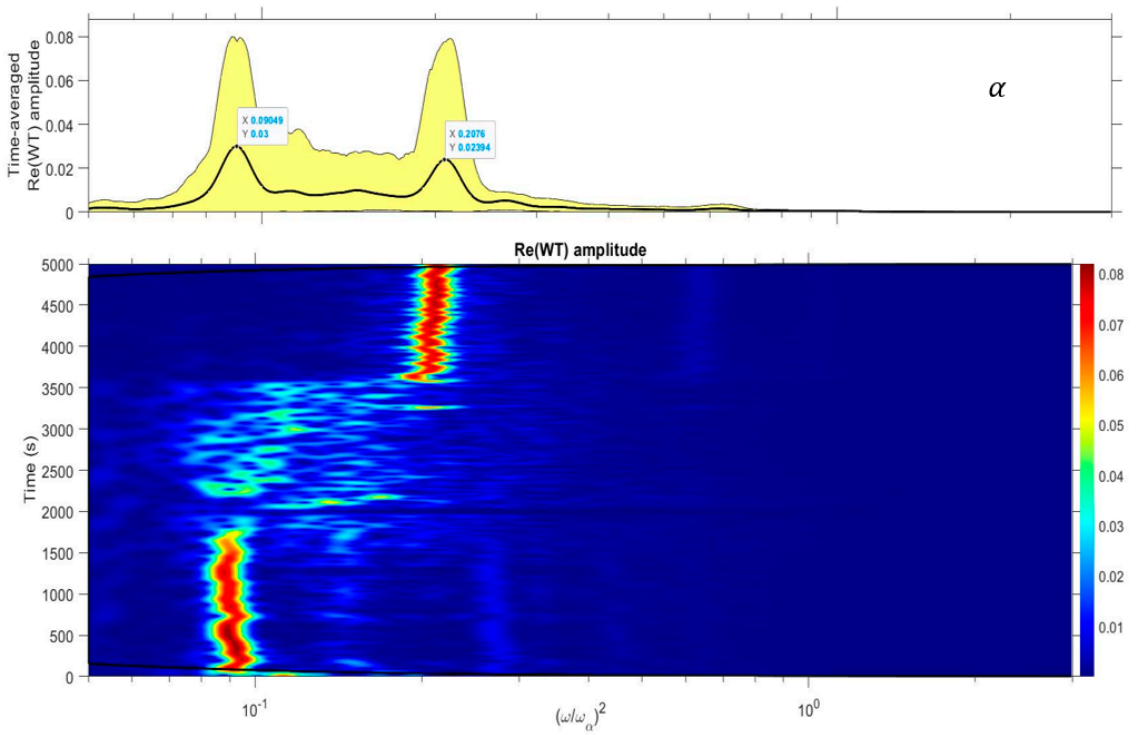

Figure 9. Time–frequency analysis of pitch displacement signal ($Q_o = 9$).

Figure 10 shows the aeroelastic response at $Q_o = 15.6$. Included in this plot is the Hilbert envelope function of the pitch displacement signal. There are four resonance captures in the cascade, which are indicated by numbered rectangles with arrows pointing to specific time locations on the envelope function. The envelope function generally takes the shape of the time–frequency representation. The blue dashed arrows denote the system jump/bifurcations. From $t = 0$ to ~500, the wing vibrates at a frequency ratio of ~0.097. The system jumps to a frequency ratio of ~0.1659 (1), followed by a jump to ~0.2403 (2). The longest of the captures in the cascade begins at $t = 1000$ and terminates at $t = 1500$ exactly; this resonance capture occurs at a frequency ratio of ~0.3154 (3). The system then jumps down to ~0.2403 (4) and then transitions back to a frequency ratio of ~0.097; the amplitude of the pitch signal shows a decrease from $t > 1500$ (see Figure 10). The time–frequency analysis for the pitch displacement signal reveals that the resonance captures 2 and 3 have the most spectral energy. The time–frequency analysis for the bending displacement signal (Figure 11) shows that the spectral energy decreases significantly after $t = 1000$, indicating that nonlinear absorption has taken place. In the time domain, the amplitude of the bending displacement signal shows a reduction beginning at $t \sim 753$. When the wing jumps to a new resonance capture, the wing exhibits a pulse-like signature (indicated by the dashed ellipses—Figure 10). The prescribed perturbation signal causes the torsional displacement dynamics to behave like a nonlinear energy sink, and the corresponding mechanism of vibration suppression is the resonance capture cascade, as demonstrated in Figure 12. The resonance captures begin to appear when the airspeed parameter is set to a value of 9; the control perturbation signal inhibits the chaotic dynamics but does not suppress the limit cycle oscillation (LCO). In Case II, it will be demonstrated that the prescribed control perturbation signal induces the second type of resonance capture, namely the *isolated resonance capture*.

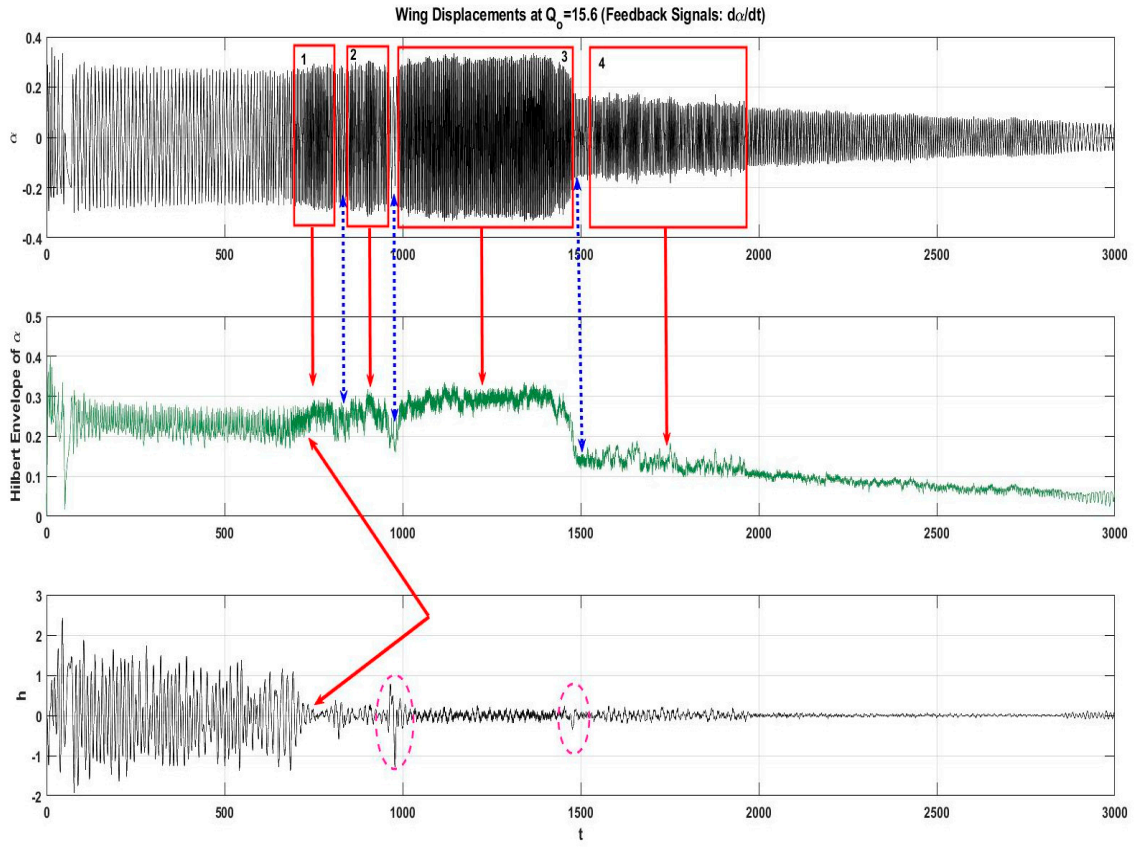

Figure 10. Aeroelastic response with resonance capture cascade ($Q_o = 15.6$).

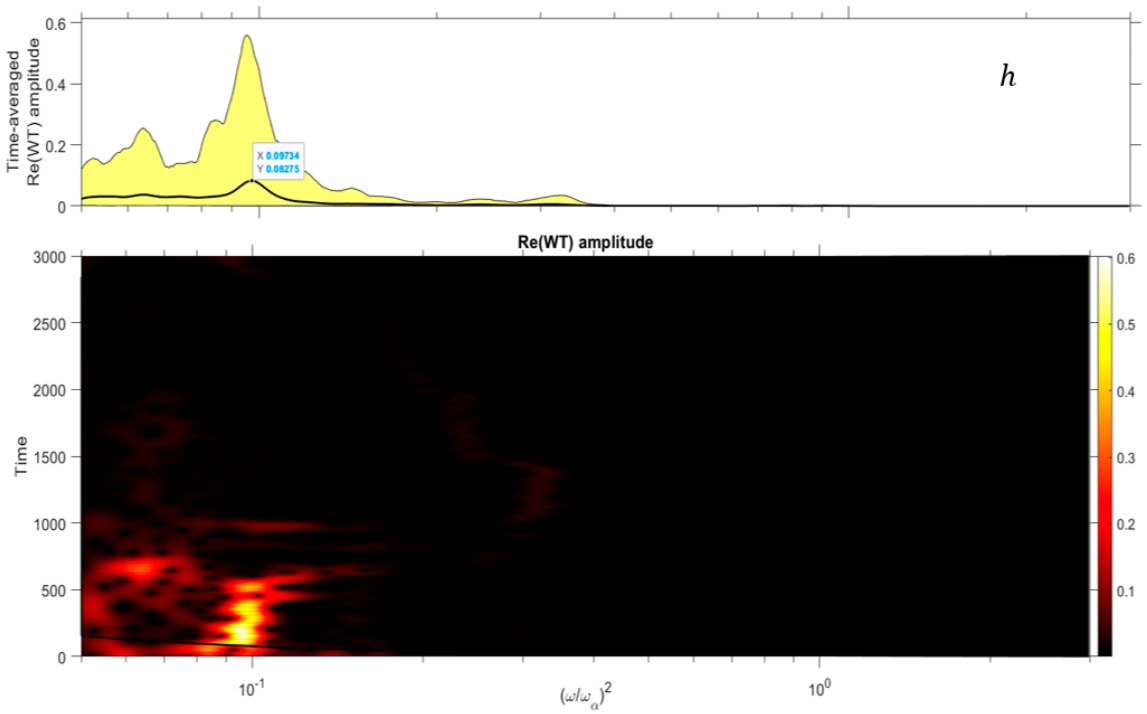

Figure 11. Time–frequency analysis: Bending ($Q_o = 15.6$).

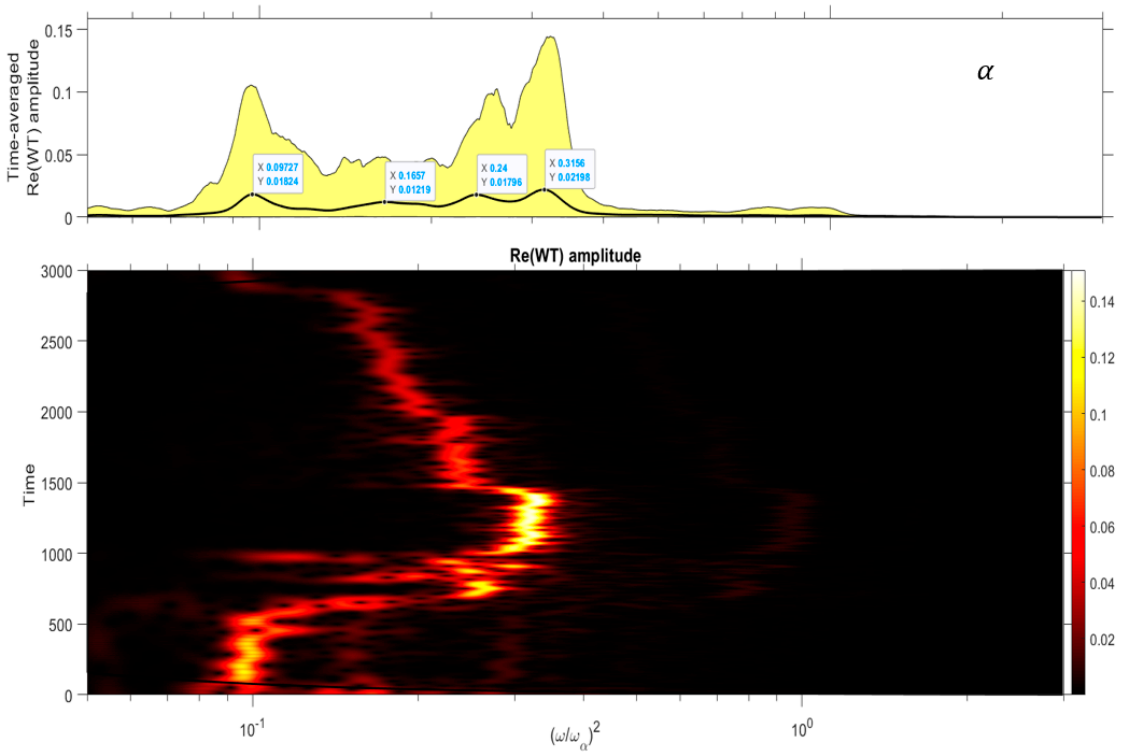

Figure 12. Time–frequency analysis: Pitch ($Q_o = 15.6$).

Case II: $\boldsymbol{Q_e = Q_o\left[cos(\dot{\alpha}t) + sin(ht)\right]}$

The control action is engaged at $t = 0$ at $Q_o = 15.6$. It is observed that the pitch and bending transient oscillations are well-damped and reach an equilibrium position of (0,0) at $t \sim 500$ (Figure 13). Both degrees of freedom are parametrically excited by the same control signal; thus, there is no energy transfer between the coupled aeroelastic displacements (i.e., the amplitude of one degree of freedom decreases while the other increases). The effective airspeed parameter Q_e timeseries shows two different regimes; when $t <$ ~812, there is a spike train with an irregular amplitude that terminates at $t \sim 812$. When $t > 812$, the control signal amplitude becomes constant ($Q_e \sim 10$). The spike train can be interpreted as the closed-loop system *hunting* for and approaching what appears to be a stable fixed point. During initial simulation runs, a saturation block was applied to the control perturbation signal; it was found that if the saturation boundaries are increased, the spike train persists to $t = 2500$, after which it is again replaced with a multiharmonic limit cycle oscillation. There is no significant change in the observed aeroelastic response, which remains stabilized. The final configuration of the saturation boundaries is set at $Q_e \pm 30$; when this is done, the spike train reported in the results only persists to $t \sim 812$ as reported above. Therefore, *the approach time* to the stable fixed point shows a sensitivity to the saturation boundaries placed on the control perturbation signal. In order to understand why the linear combination of harmonic feedback signals is effective in fully suppressing the vibration of the airfoil, the individual effect of each harmonic feedback signal must be examined. For the term $Q_e = Q_o[\sin(ht)]$, the time–frequency analysis (Figure 14) reveals that there are two frequency ratios at ~0.071 and at ~0.1712. The frequency ratio at ~0.071 is closest to the calculated parametric antiresonance ratio of 0.0763 given in Table 1; this mode is also close to the fundamental frequency ratio of ~0.09259 identified in the time–frequency analysis of the uncontrolled dynamics (both pitch and plunge; see Figures 5 and 6). The magnitude of the wavelet transform coefficient is low at ~0.1712 and is closest to 0.1877, the difference between 0.2803 and 0.09259. Note again that ~0.09259 and ~0.2803 have a significant amount of energy indicated by the corresponding wavelet transform coefficients. Note that there are no spectral moments beyond ~0.1712.

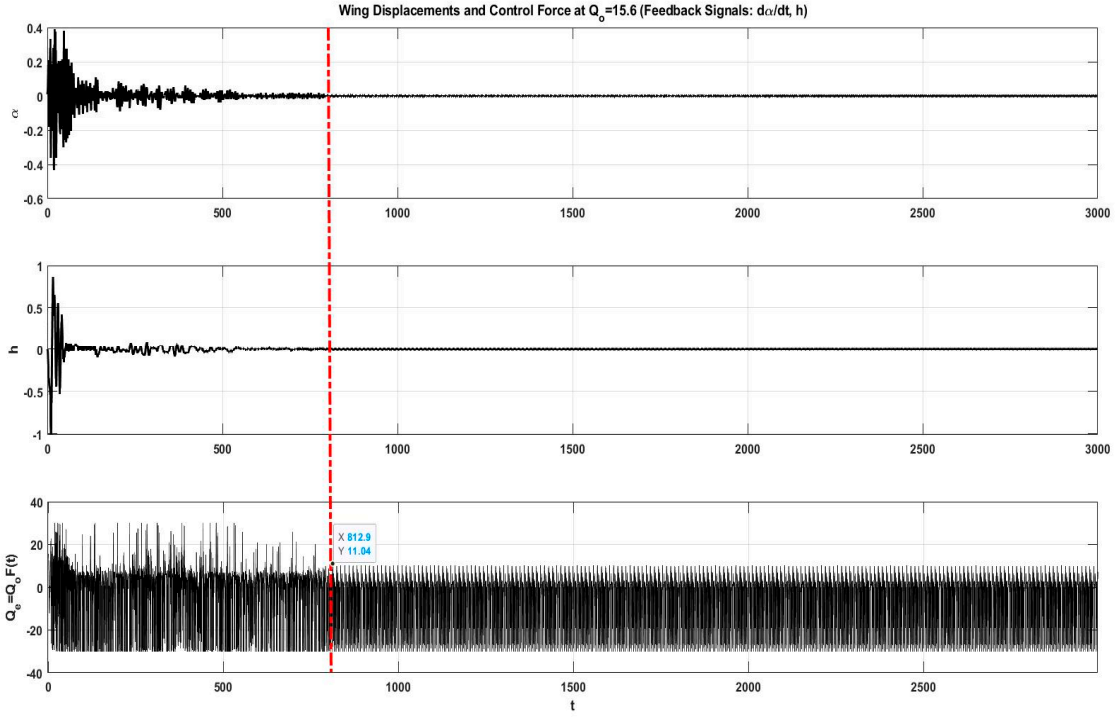

Figure 13. Closed-loop aeroelastic response ($Q_e = Q_o\left[\cos(\dot{\alpha}t) + \sin(ht)\right]$, $Q_o = 15.6$).

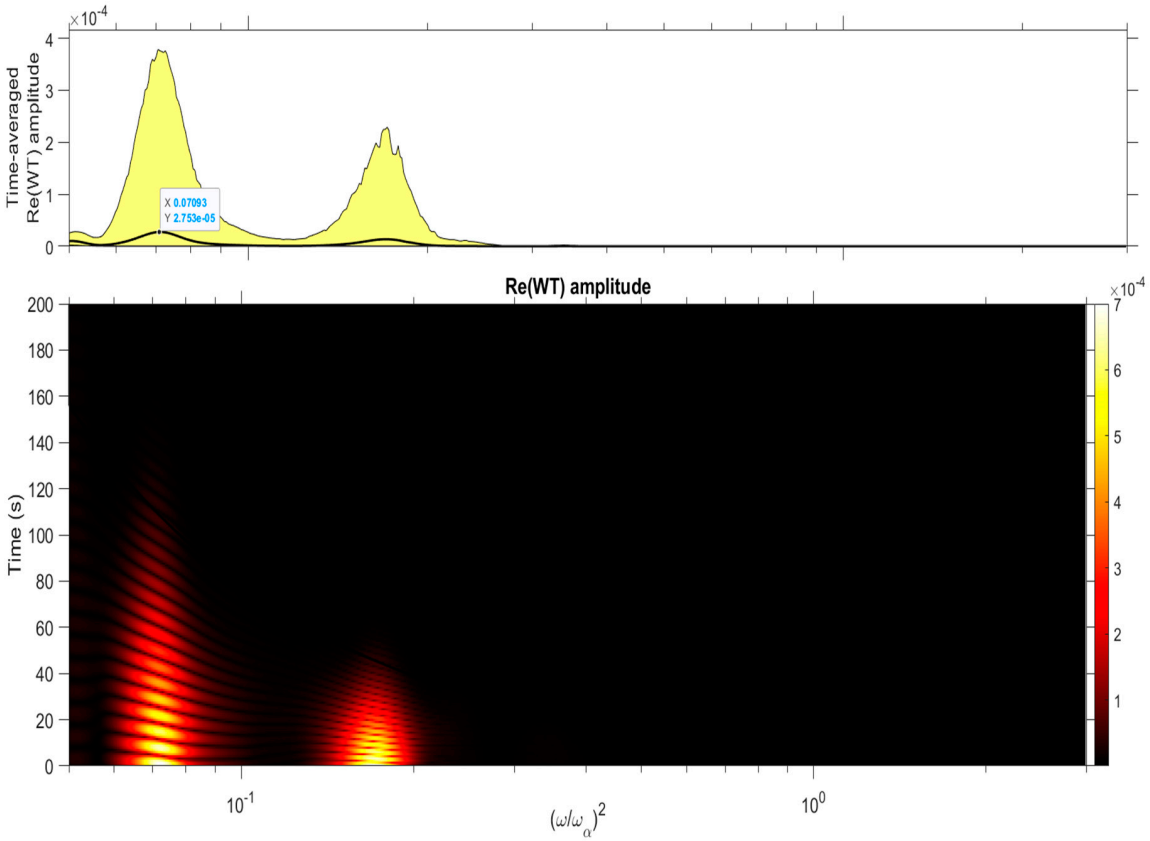

Figure 14. Time–frequency analysis: $Q_e = 15.6[\sin(ht)]$.

For the term $Q_e = Q_o\left[\cos(\dot{\alpha}t)\right]$, the reader will note that for frequency ratios less than ~0.1947, the wavelet transform coefficient spectra are flat (Figure 15). For frequency ratios greater than ~0.1947,

the spectra are broadband all the way up to a frequency ratio of 2, which is closest to the parametric antiresonance ratio of 2.0951 given in Table 1. When these two harmonic feedback terms are combined, what results is a control perturbation signal that covers the entire bandwidth of the aeroelastic system. The cosine term on its own induces a resonance capture cascade that is characteristic of a nonlinear energy sink; it does so in the absence of spectral information from the bending degree of freedom, which happens to contain two energy-rich frequencies. A time–frequency analysis of the combined control perturbation signal (Figure 16) reveals that there are several spectral peaks in the wavelet coefficient spectra that correspond to the lines of constant frequency in the wavelet-based spectrogram. The strongest of these occurs at a frequency ratio of ~0.2591, slightly less than the uncontrolled parametric resonant peak at ~0.2803 identified in Figure 5; in the uncontrolled spectra of the pitch displacement signal, this mode (~0.2803) was weaker in power than the parametric antiresonant mode at ~0.09259. The peak at ~0.08621 (closest to ~0.09259 and 0.0763—see Table 1) is slightly weaker in power at a wavelet transform coefficient magnitude of 1.959 compared to 2.725 at ~0.2591. Note also the difference mode at ~0.1724; this mode is the difference between ~0.2591 and ~0.08621, and is an indication of nonlinear frequency interaction.

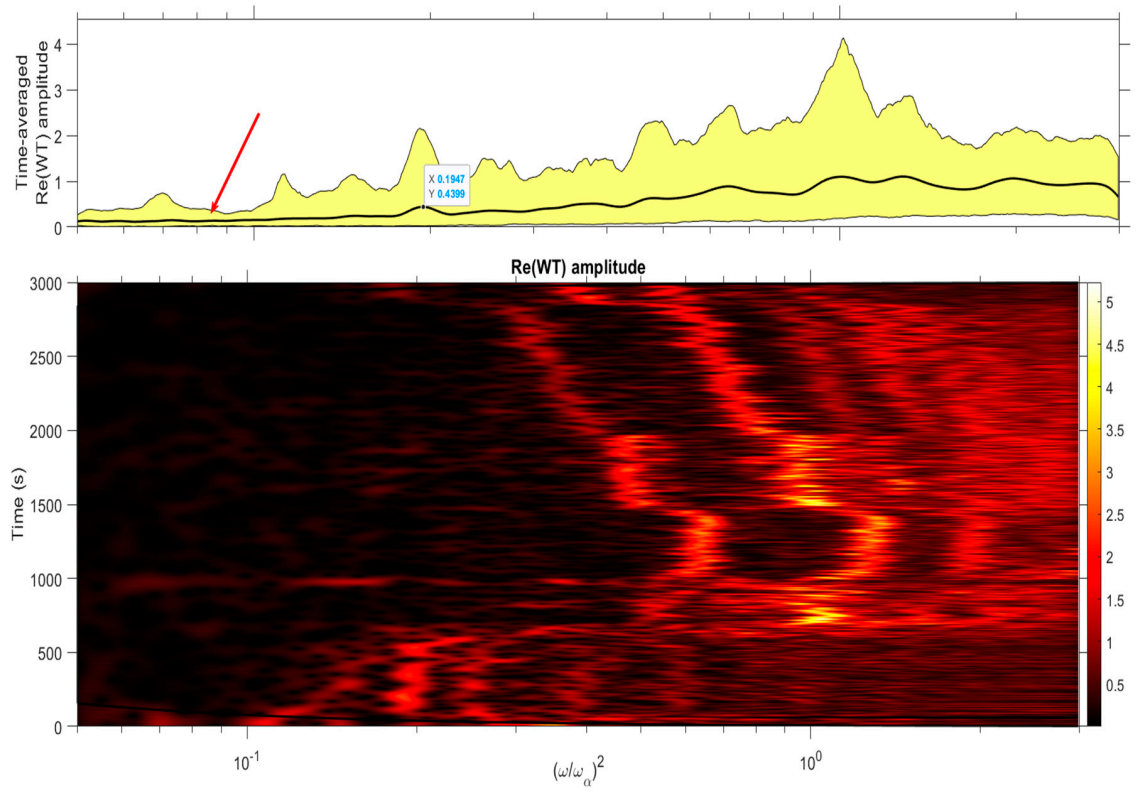

Figure 15. Time–frequency analysis: $Q_e = 15.6\left[\cos(\dot{\alpha}t)\right]$.

Note that when $t <$ ~812, the energy is diffuse, which corresponds to the spike train observed in the time series after which the time frequency map becomes highly organized about specific frequency ratios. It is also important to notice the regions of the map where there are no distinct frequency bands or peaks in the spectra (see red arrows—Figure 16); these regions are flat and fall between three distinct frequencies. This is caused by the application of the first-harmonic feedback term. For frequency ratios greater than ~0.2591, the reader will notice that the tones are closely spaced and cover a wide band of frequency ratios of both species. In addition to the above, the control perturbation signal changes sign and crosses the zero axis; these sign changes and zero crossings without the adverse transients (sometimes seen in state-switched devices) aid in increasing the damping of the system. The overall effect of the combined perturbation signals on the aeroelastic system is shown

in the time–frequency domain (Figure 17). This figure shows the time–frequency maps for (a) pitch, (b) plunge, and the (c) control perturbation signal (revisited) in a column. The reader will note that the black dashed line is centered on the difference mode of ~0.1724 and is the dividing line between the low-frequency components and the high-frequency components. To the left of the line, the effect of the sinusoidal feedback signal can be seen. For the pitch displacement signal (Figure 17a), there are weak spectral moments at $t < 100$ and between $t = 200$ and 300. The low magnitude of the wavelet transform coefficients indicates minimal energy exchange between the pitch and plunge degrees of freedom; hence, there are no shared or common sustained frequencies in the low-frequency band as compared to the uncontrolled dynamics that vibrate at a frequency ratio of 0.09259 (see Figures 5 and 6). To the right of the line, we see that the control perturbation signal induces frequency entrainment about the ratio ~0.2591 and suppresses the remaining high-frequency components. There is no significant energy exchange in this frequency band between the aeroelastic displacements. The plunge displacement signal (Figure 17b) shows a spectral lobe indicative of a short-duration resonance capture with an escape at $t \sim 100$. To the right of the line, there are no spectral moments. The presence of particular frequency components contained in the control perturbation signal means that these frequency components will be attenuated or suppressed in the closed-loop system dynamics while inhibiting nonlinear energy absorption or exchange, which results in the quenching of the aeroelastic displacements. The mechanism of vibration suppression is an isolated resonance capture, which occurs at a frequency ratio of ~0.2951 followed by an escape from resonance capture.

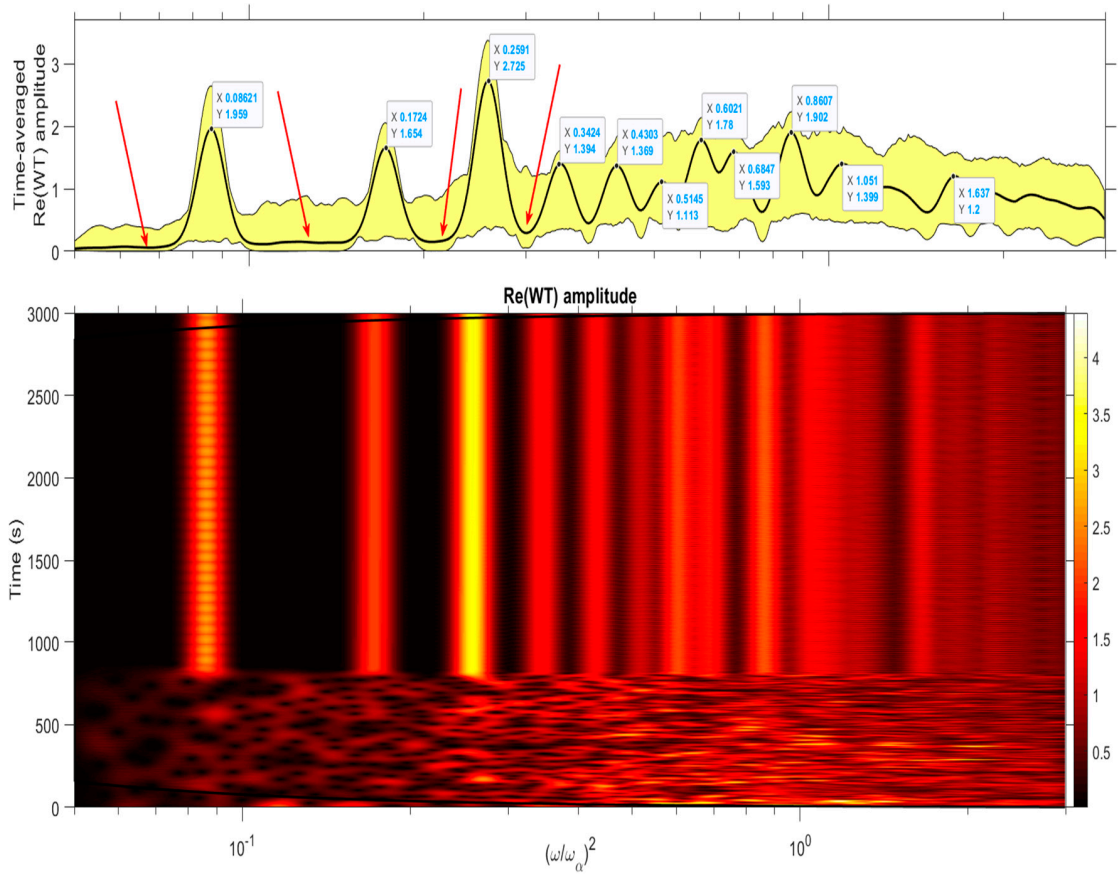

Figure 16. Time–frequency analysis: $Q_e = 15.6\left[\cos(\dot{\alpha}t) + \sin(ht)\right]$.

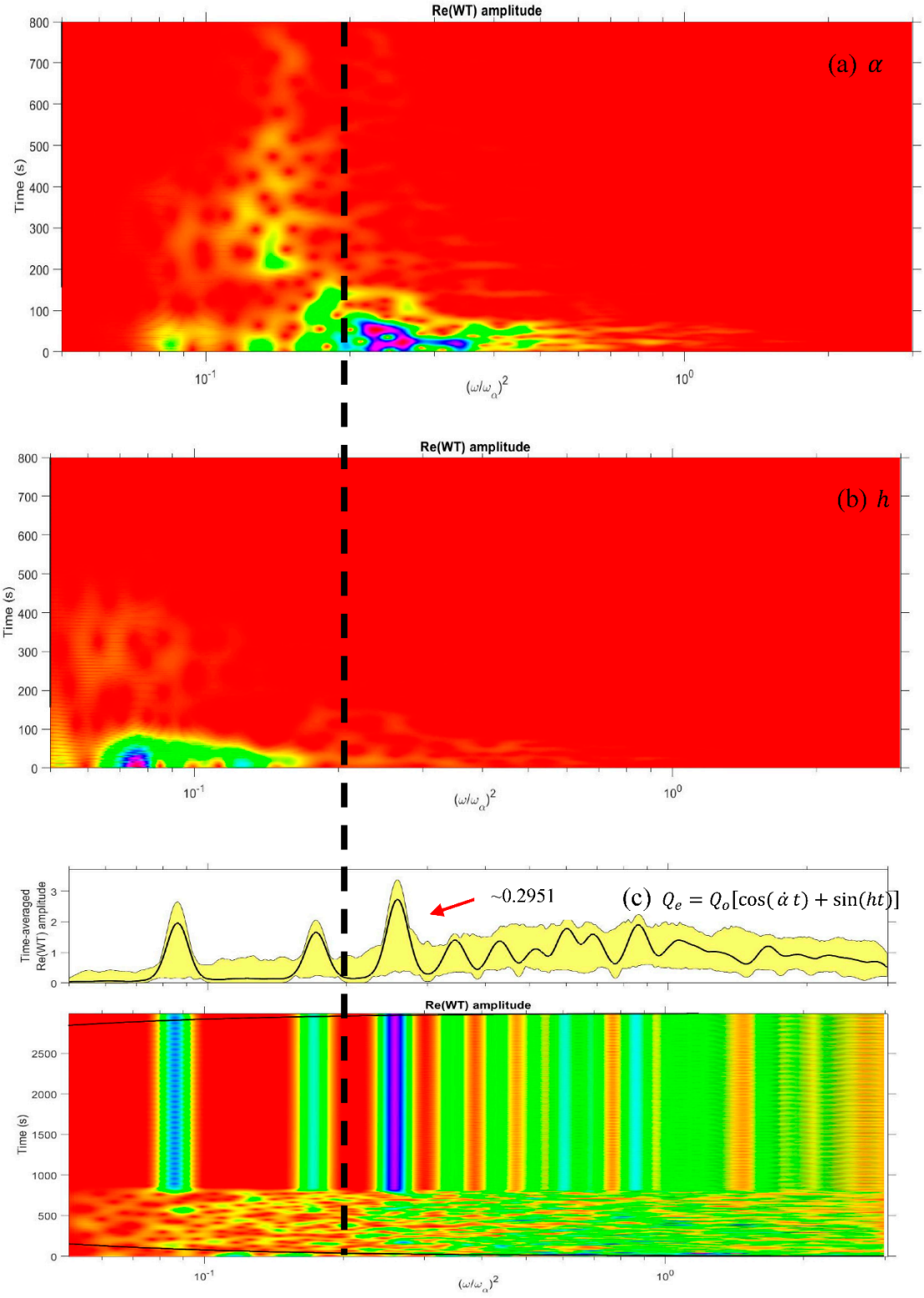

Figure 17. Overall effect of control perturbation signal of system dynamics ($Q_o = 15.6$). (**a**) Time frequency analysis of the bending (h) dof. (**b**) Time frequency analysis of the pitch (α) dof. (**c**) Time frequency analysis of the prescribed perturbation signal. Note that the perturbation signal contains spectral components not present in the time frequency analyses of the aeroelastic displacements.

For $Q_o = 5$, located around the Hopf bifurcation boundary, it is again observed that the pitch and bending transient oscillations are well-damped and reach an equilibrium position of (0,0) by $t \sim 500$ with no energy exchange between the coupled aeroelastic displacements (Figure 18). Notice that the control perturbation signal does not transition to a multiharmonic limit cycle like the previous case, but remains as a time-continuous spike train. It can also be observed that the control perturbation signal adjusts in amplitude and frequency to maintain the stable aeroelastic response. The time–frequency analysis (Figure 19) reveals that there are several frequency ratios, namely ~0.1452, ~0.2295, ~0.2903, and ~0.8364. All these frequency ratios show weak and intermittent periodicity. Of note are the frequency ratios ~0.2295 and ~0.2905; they are closely spaced together and show signs of nonlinear frequency interaction. The frequency ratio ~0.2295 is closer to the parametric resonance ratio of 0.2, and ~0.2905 is closer to the parametric antiresonant frequency ratio of 0.3053 listed in Table 1. There are no flat regions in the wavelet coefficient spectra and the spectra are broadband. There are no sharp spectral peaks, because the energy is distributed among the frequency components present at the Hopf bifurcation condition.

Figures 20 and 21 show a comparison between the controlled and the uncontrolled dynamics at both operating conditions. The figures show that the prescribed control law is effective in suppressing the wing vibrations as compared to the uncontrolled dynamics. Figure 22 demonstrates that when the controller is switched on at $t = 1500$, the closed-loop system is successfully damped despite the fully developed dynamics in the chaotic regime.

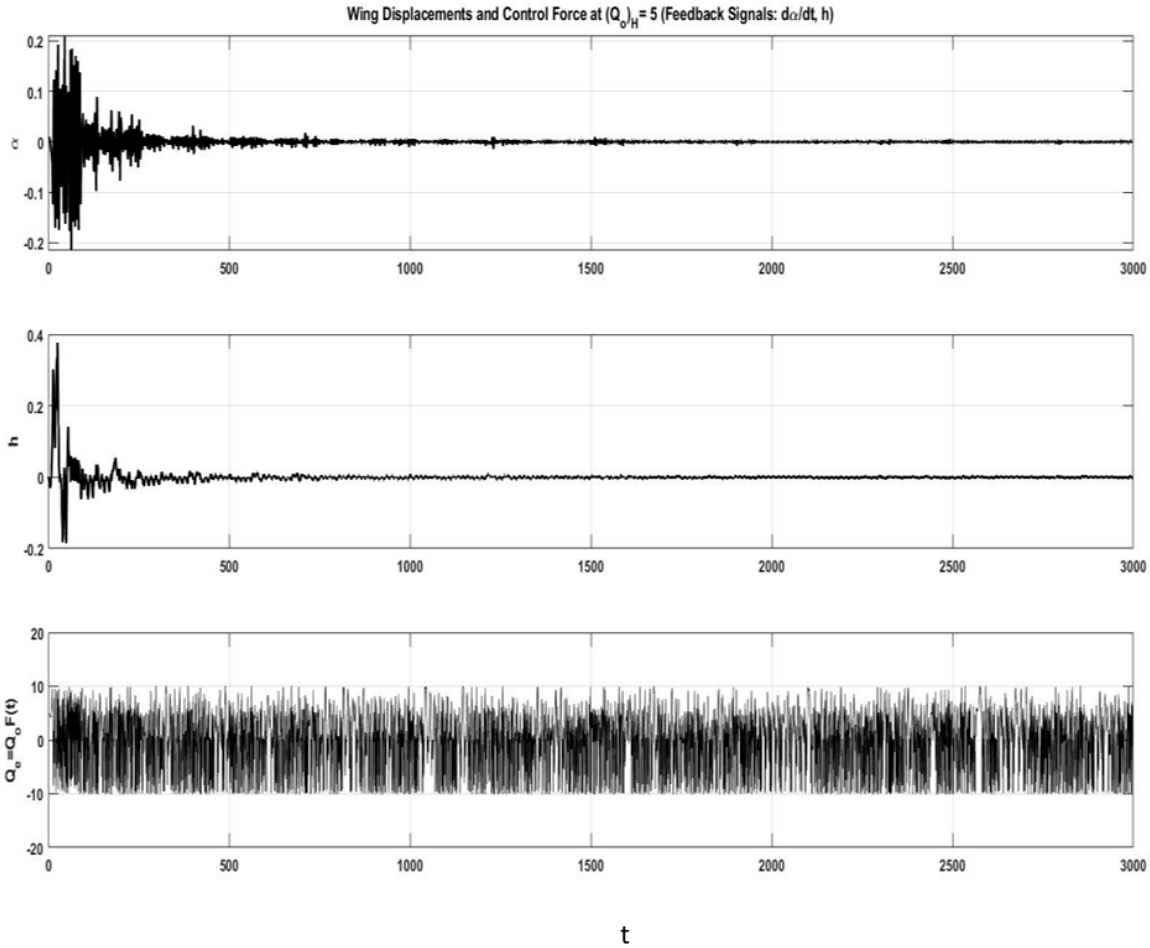

Figure 18. Closed-loop aeroelastic response ($Q_e = Q_o\left[\cos(\dot{\alpha}t) + \sin(ht)\right]$, $Q_o = 5$).

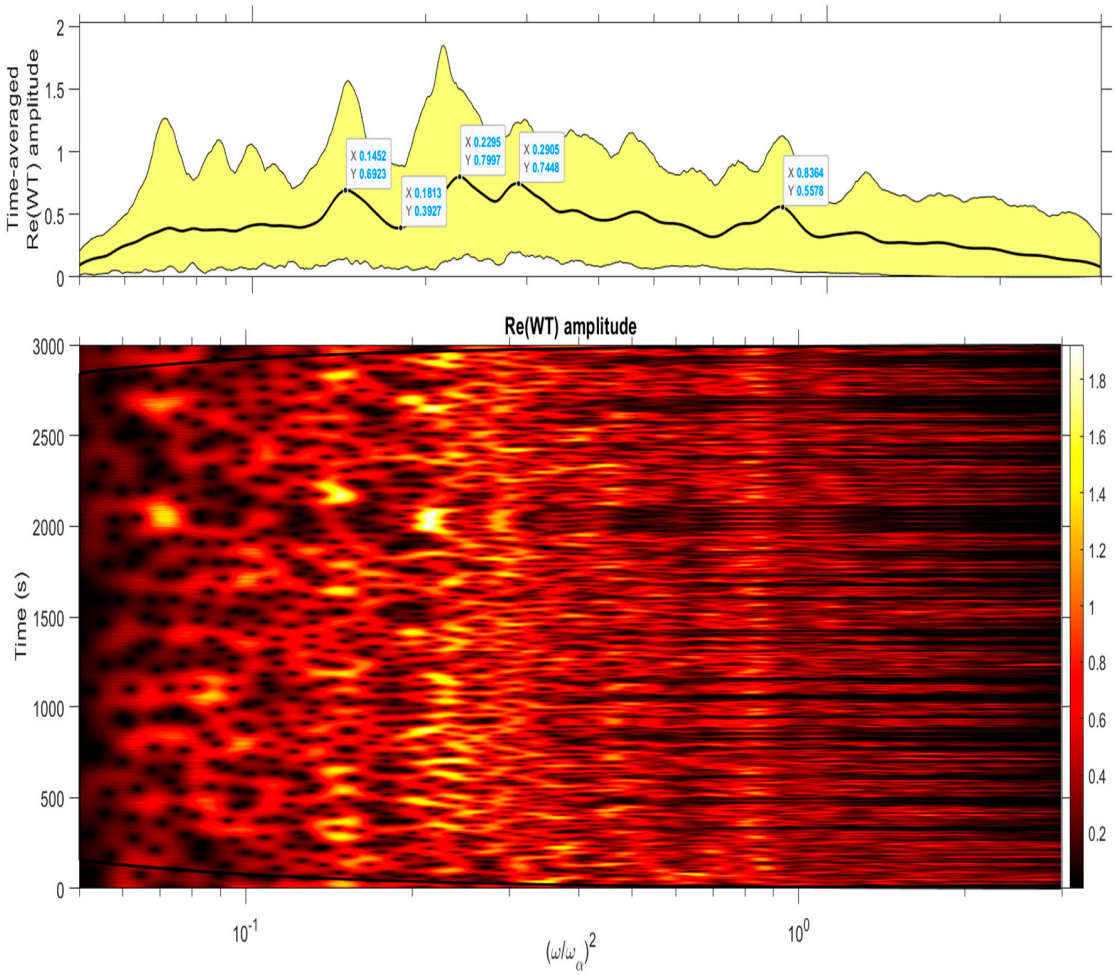

Figure 19. Wavelet time–frequency analysis: Control perturbation signal ($Q_o = 5$).

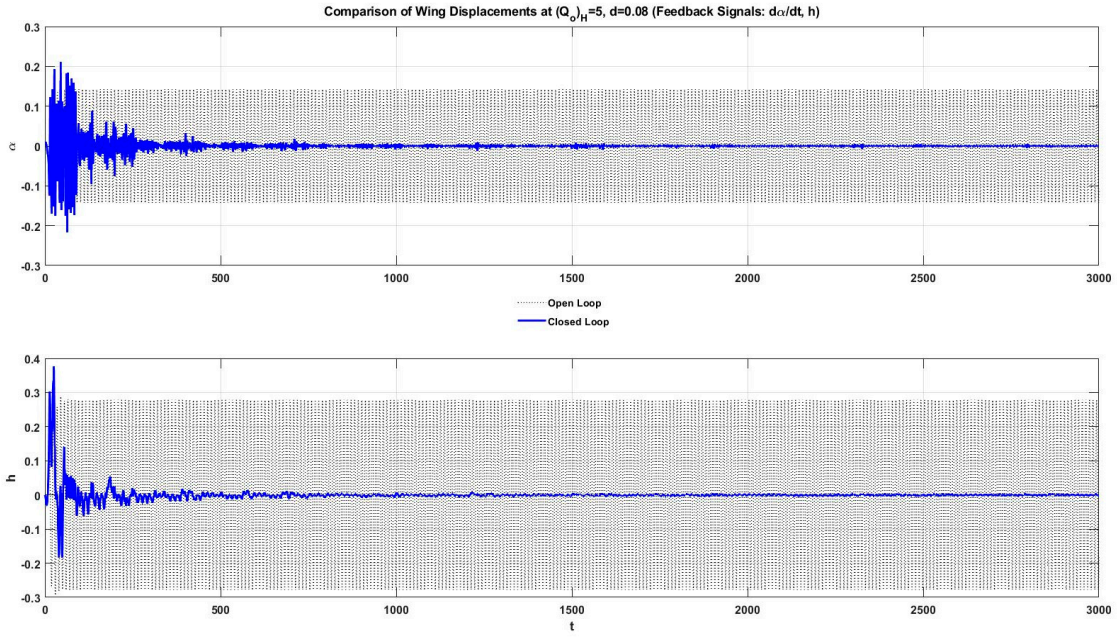

Figure 20. A comparison of aeroelastic responses ($Q_o = 5$).

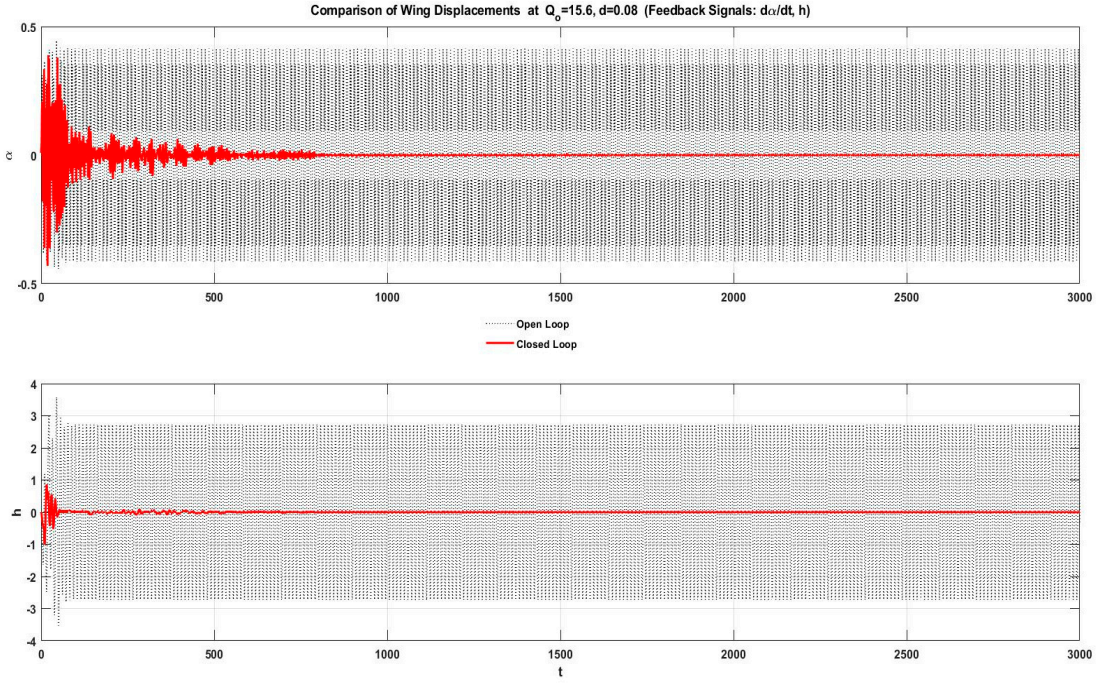

Figure 21. A comparison of aeroelastic responses ($Q_o = 15.6$).

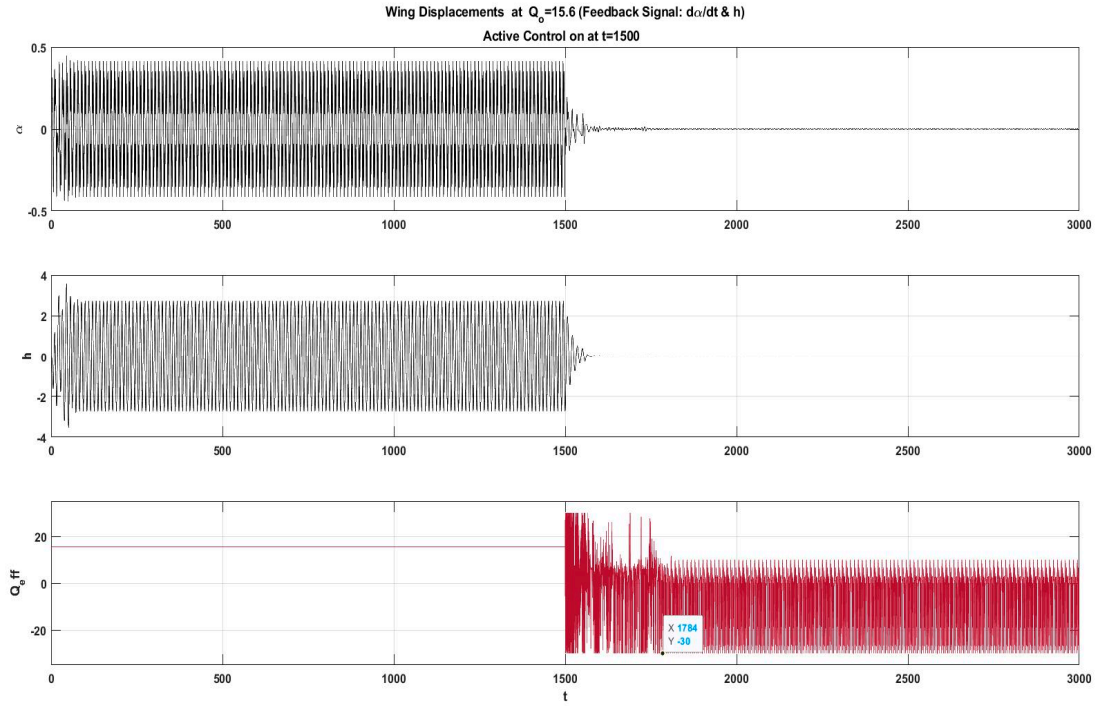

Figure 22. Aeroelastic response to control at t = 1500.

Figure 23 shows that the Hilbert envelope functions for each of the airspeed parameter settings are superimposed on one another. The envelope functions collectively show that the control action is able to damp the oscillations rapidly across a wide range of airspeed parameter settings including the Hopf bifurcation condition and in the post-flutter (chaotic) regime. The reader will note the dashed (red) curve enveloping the amplitude functions; this curve is used to obtain the instantaneous system damping (Figure 24). There are three distinct time intervals on this plot; the first interval is indicated by a blue double arrow, where the slope between t = 39.5 and 72.6 is high, indicating that the damping

ratio is large. The damping ratio changes again (black dashed double arrow) at t = 72.6, where the damping ratio decreases as the controller dissipates the energy because the system now requires less damping. The system damping changes for the final time at t = 383, where the slope on this interval is shallow, so less damping is needed here as the pitch amplitude has fallen below 0.1. The damping between t = 383 and 450 is less than the previous two regions.

For Case II, we have seen that the linear combination of harmonic feedback signals involving the angular velocity and bending displacement can fully suppress the vibration of the wing. The prescribed perturbation signal simultaneously inhibits the multimodal energy absorption mechanism (caused by the cosine term) while providing the conditions for frequency entrainment in the lower frequency band (caused by the sinusoidal term). The frequency entrainment is caused by the closed-loop vibration mode closest to the fundamental tones identified in Figures 5 and 6. It has also been observed that the sinusoidal term has a strong effect on the first term of the perturbation signal and is the reason for the short-duration resonance captures. The effects of the control perturbation signal examined in Cases I and II are summarized in Figure 25. These short-duration resonance captures are responsible for the minimal energy exchange between the pitch and bending DOFs as seen in Figure 25. The short-duration resonance capture occurs about a single frequency ratio of ~0.2951, which makes it an isolated resonance capture.

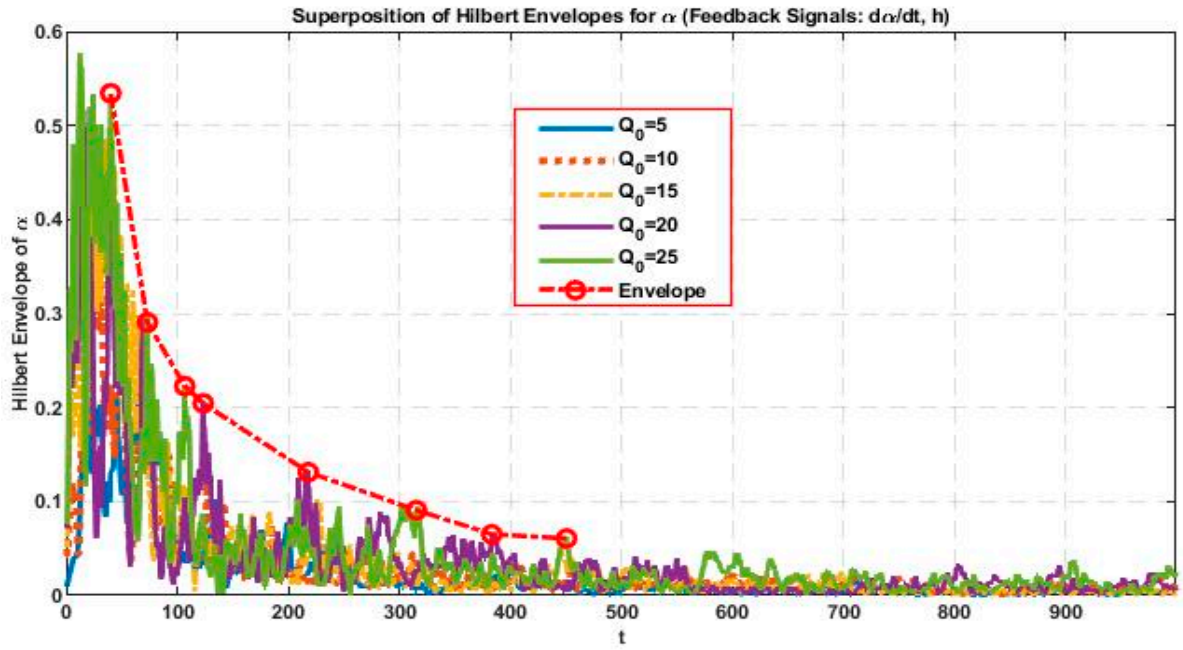

Figure 23. Amplitude function for different values of Q_o.

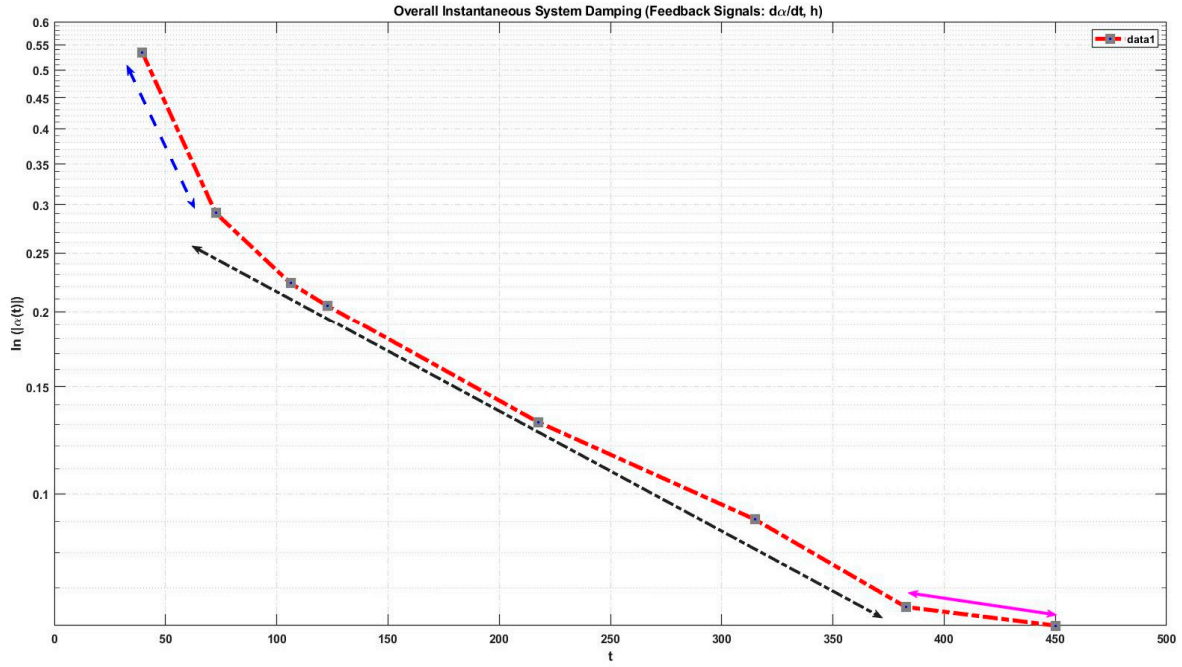

Figure 24. Instantaneous system damping.

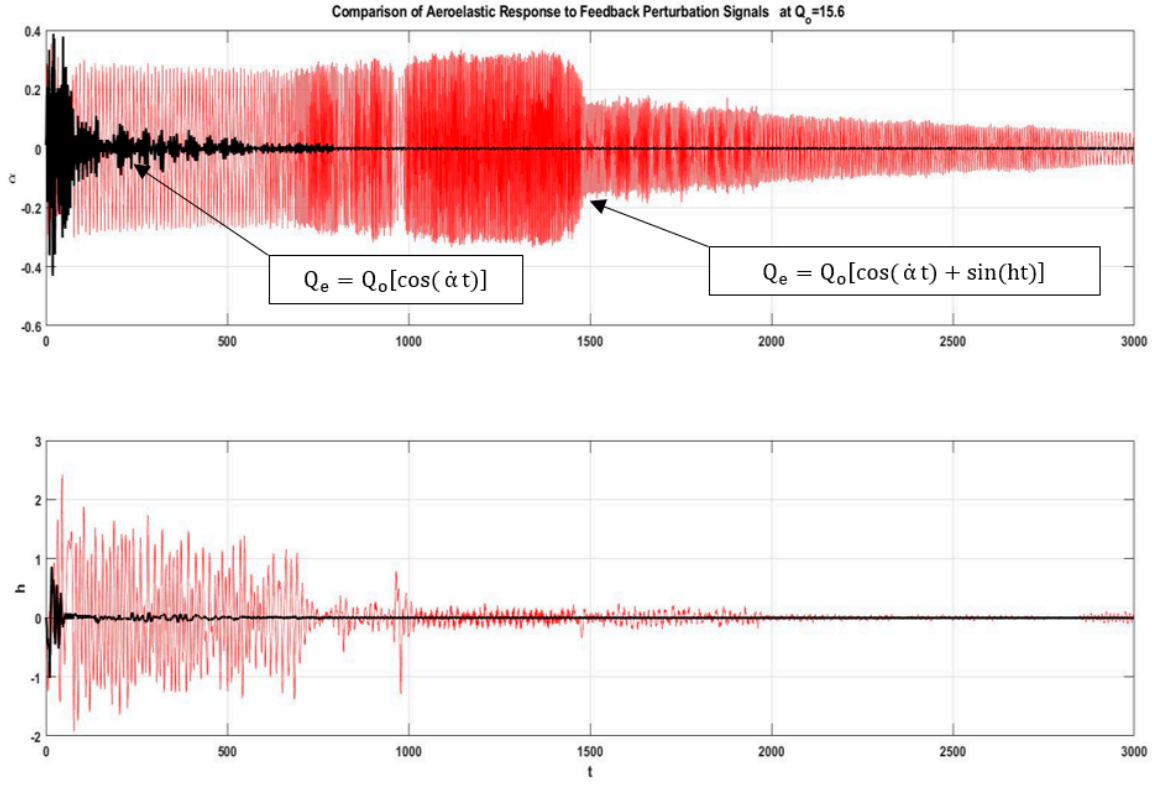

Figure 25. Effect of perturbation signals of aeroelastic response.

Case III: Effect of random excitation on the aeroelastic responses of the wing (open- and closed-loop)

Aircraft in general (and, in particular, high-performance aircraft) experience nonlinear aeroelastic phenomena inside their published operational flight envelopes due to excitation by turbulence [21,22]; this can become a significant airworthiness issue if not accounted for in the design, development, and certification of the aerospace structure itself and the resulting aeroelastic control laws. The purpose

of this section is to briefly examine the effects of random excitation (simulated turbulence) on the uncontrolled and closed-loop aeroelastic system. Liu et al. [23–25] present work on a 2D airfoil with cubic nonlinearities in both bending and torsion; one of the works has the wing under sliding mode control. The general objective of these works was to examine the effects of combined harmonic and random excitation at various noise intensities on the aeroelastic response of the airfoil. However, only the pitch degree of freedom was subject to excitation. From a practical standpoint, turbulence is felt by the airfoil as external forcing and a parametric excitation. Specifically, for a typical section, the oncoming freestream velocity vector that interacts with the airfoil is augmented by longitudinal and vertical turbulence (Figure 26).

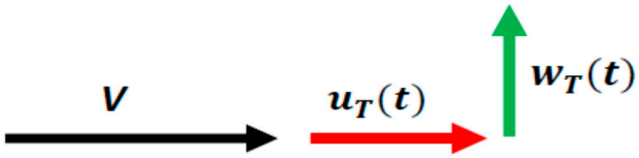

Figure 26. 2D turbulence components.

The schematic below (Figure 27) shows the interaction between the aeroelastic forces and turbulence via a feedback loop; the aerodynamics block is further divided into two blocks, with the first block as a function of the longitudinal turbulence, and vertical turbulence acting as an input to the global aerodynamics. The airfoil block is essentially subjected to three inputs: The two components of aerodynamics, which include the turbulence components, and an input designated as external forcing (which could be a gust or harmonic excitation). Therefore, in this paper, the simulation will be updated such that the coupled bending and torsional dynamics will be subjected to random excitation in the chaotic regime (Q_o = 15.6). The parameter ν is the noise intensity, typically ranging from 0 to 1, and η(t) is the Gaussian random excitation (see Equation (10)).

$$\begin{aligned} \ddot{h} + 0.25\ddot{\alpha} + 0.1\dot{h} + 0.2h + 0.1Q\alpha &= \nu\eta(t) \\ 0.25\ddot{h} + 0.5\ddot{\alpha} + 0.1\dot{\alpha} + 0.5\alpha + e\alpha^3 - dQ\alpha &= \nu\eta(t) \end{aligned} \tag{10}$$

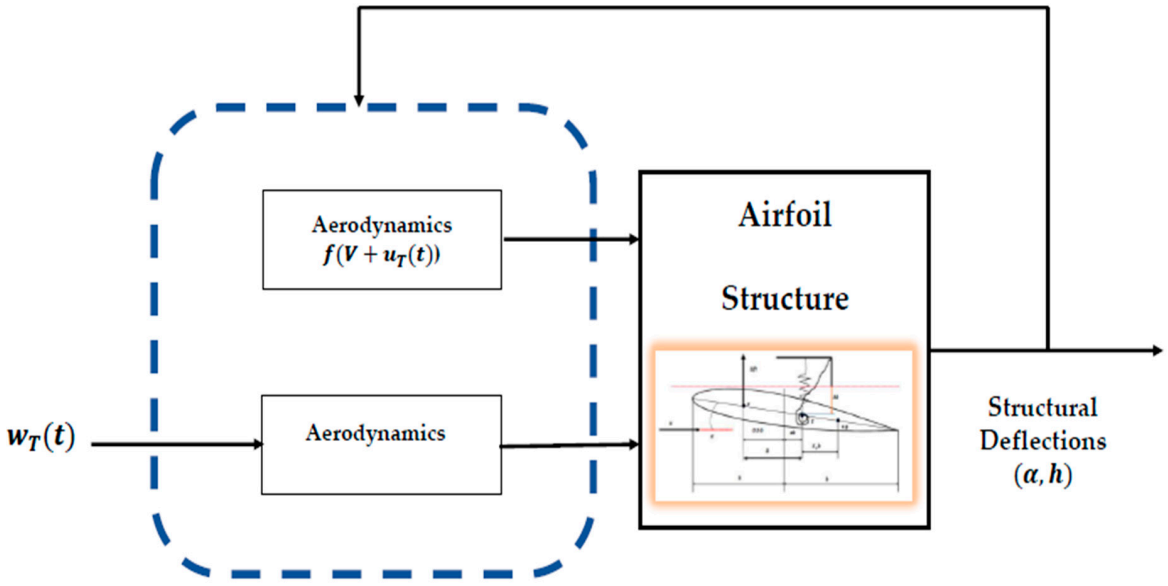

Figure 27. Aeroelasticity–turbulence interaction schematic.

Figure 28a,b show the comparison between the amplitude-based probability density functions (PDFs) for the unforced and the noise-excited dynamics of the aeroelastic displacements. In Figure 28a, the unforced system exhibits a bimodal PDF in bending and four distinct displacement modes in pitch (Figure 28b). The multiple peaks seen in Figure 28b indicate that the system is strongly phase-coherent. When the system is excited by the noise ($\nu = 1$), it is observed that the random excitation suppresses the phase coherence (also referred to as coherent oscillation [26]); this is indicated by the single peak seen in the bending PDF and the double hump seen in the pitch PDF. The signal-to-noise ratio (SNR) becomes less than zero for noise intensities between 0.4 and 0.5.

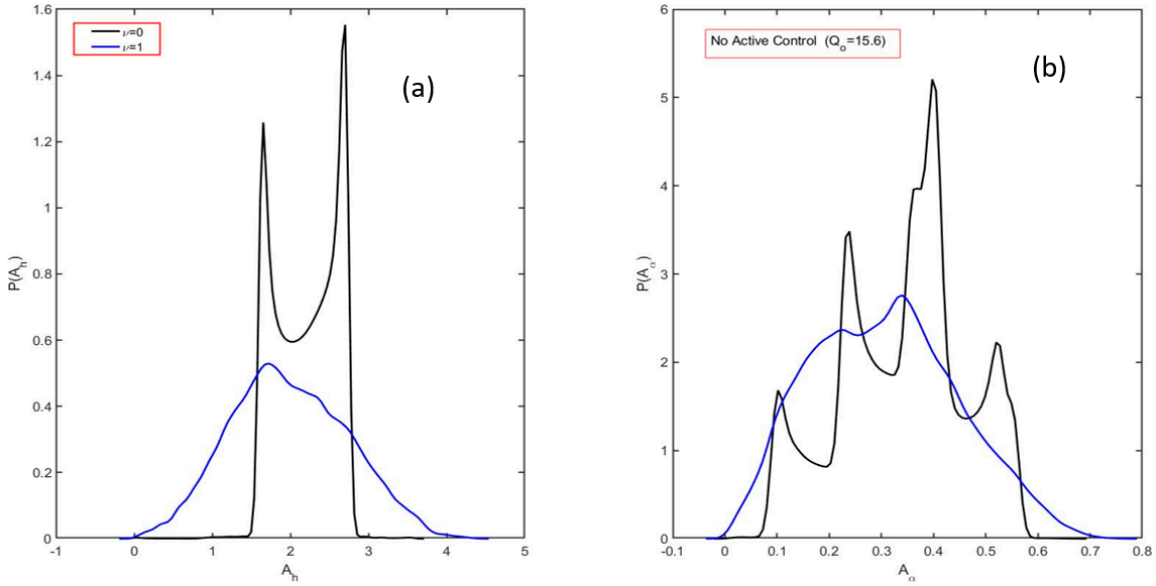

Figure 28. Probability density functions for aeroelastic displacements (open-loop, $\nu = 1$). (**a**) Comparison of bending (h) pdfs (un-forced & with random excitation). (**b**) Comparison of pitch (α) pdfs (un-forced & with random excitation). The noise intensity suppresses phase coherence.

In Figure 29, a comparison of the frequency spectra is presented for the pitch displacement. It can be observed that the excitation by noise alone results in the attenuation of higher modes (namely ~0.4657, ~0.6522, and 0.8385). Only the parametric antiresonance mode (~0.09325) and a parametric resonance mode located at ~0.2795 remain. A similar result is discussed by Ditzinger and his colleagues [26]; they have observed that random excitation alone (an uncorrelated Wiener process) caused the attenuation of frequency peaks seen in the spectra of a Langevin system, and significant reduction in the height of the main spectral peak. A time–frequency analysis of the aeroelastic displacements (Figures 30 and 31) show that the parametric antiresonance mode generally holds most of the energy while the parametric resonance mode has weak intermittent periodicity. In addition, the wavelet coefficient magnitude is higher in the linear bending dynamics at the parametric antiresonance mode (~0.09325) than in pitch due to mechanical coupling, which results in an energy exchange between the two displacements (Figure 31). For the unforced case, the results show that the excitation by noise suppresses the phase coherence. The unforced condition is a post-flutter regime and it is a condition that compromises the structural integrity of the primary flight structure; excitation by turbulence in this instance is beneficial to the wing structure (in its current aeroelastic configuration) as it suppresses the chaotic response.

Figure 32a,b presents a comparison of the aeroelastic system PDFs under closed-loop control, with and without Gaussian random excitation. Under closed-loop control alone, the PDFs are unimodal with a sharp peak in both bending and torsion about their respective equilibrium positions. When the controlled system is perturbed by the Gaussian random excitation, the PDFs show that there is diffusion at the base of the PDFs and a shift in equilibrium position; this result suggests that excitation by noise alone is destabilizing under closed-loop control. The comparison time histories

(Figures 33 and 34) show aeroelastic displacements that have been destabilized and are transformed into random limit cycle oscillations. The signal to noise ratio (SNR) becomes negative for noise intensities as low as ~0.02. A time–frequency analysis (Figures 35 and 36) shows that the excitation by noise amplifies a parametric antiresonance mode located at ~0.0721 and the parametric resonance mode located at ~0.2061. The proposed control scheme is susceptible to noise; one possible way to mitigate the destabilizing effect of noise on the closed-loop system is to apply a least-mean-square (LMS) adaptive filter to the feedback signals before they are passed to the control law itself. Further numerical experimentation is needed to tune the LMS filter parameters and generate parameter maps to accommodate the changes in the vehicle operating point, after which a re-assessment of the robustness of the proposed control scheme is required with the adaptive filter in place.

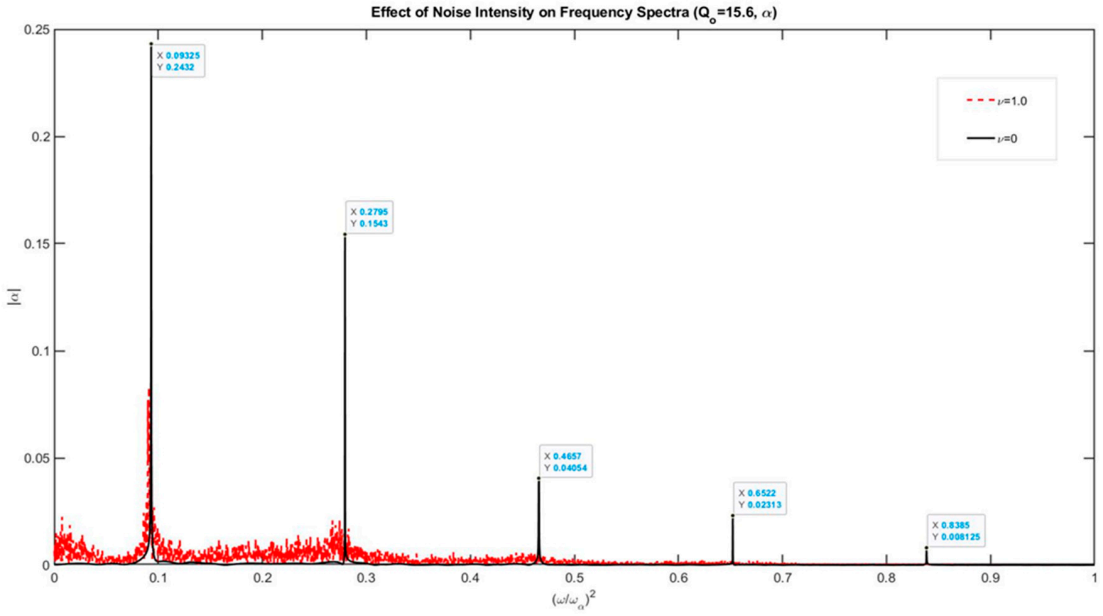

Figure 29. A comparison of frequency spectra (α).

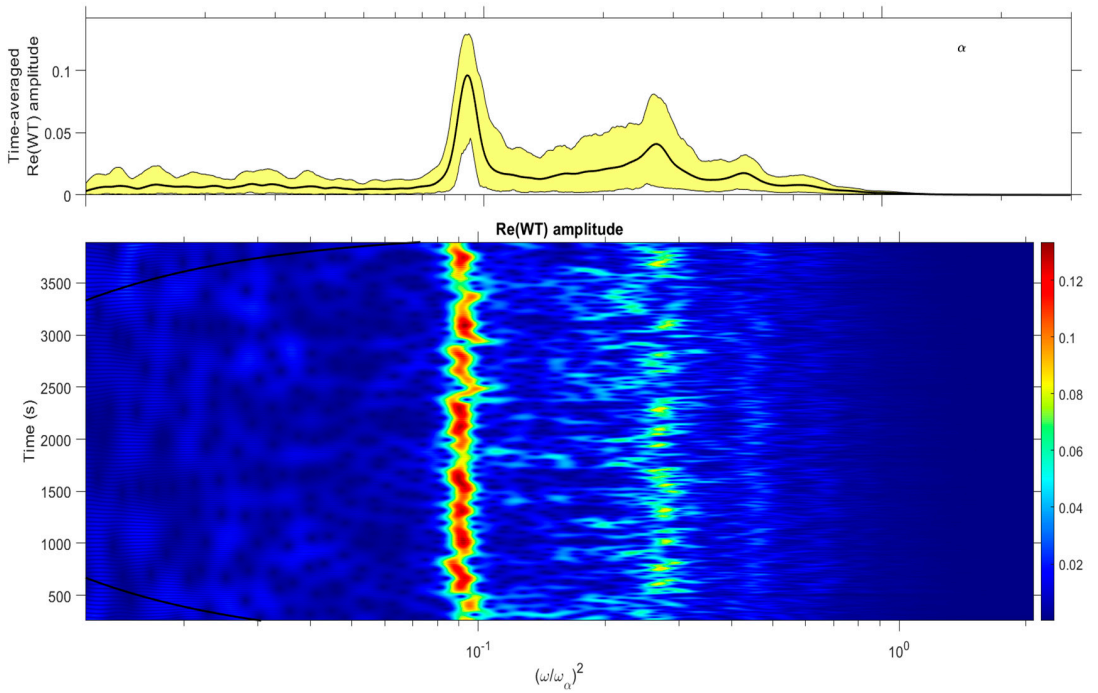

Figure 30. Time–frequency analysis (α, open-loop, $\nu = 1$).

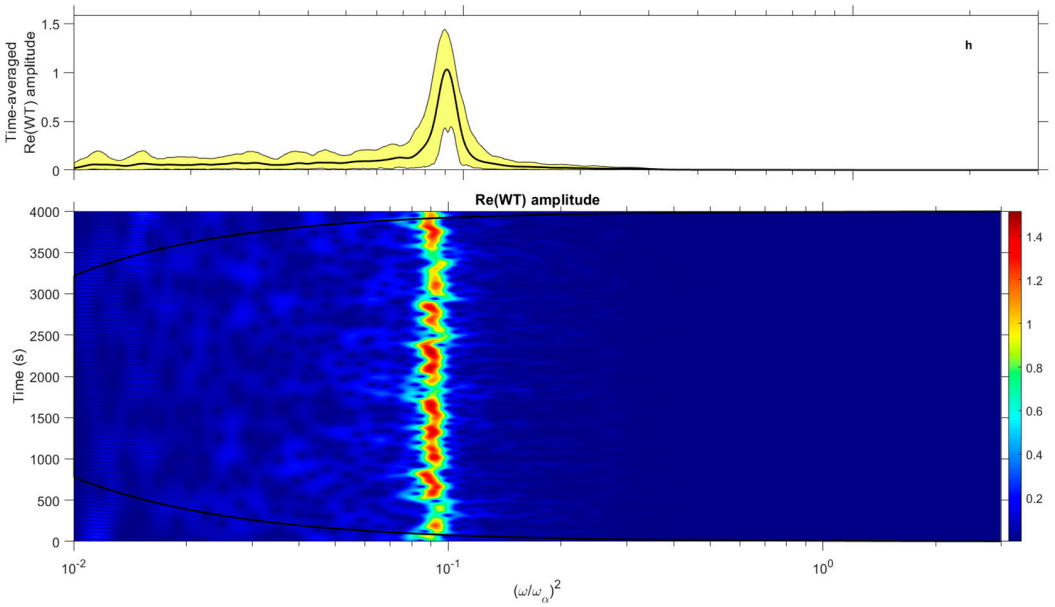

Figure 31. Time–frequency analysis (*h*, open-loop, $\nu = 1$).

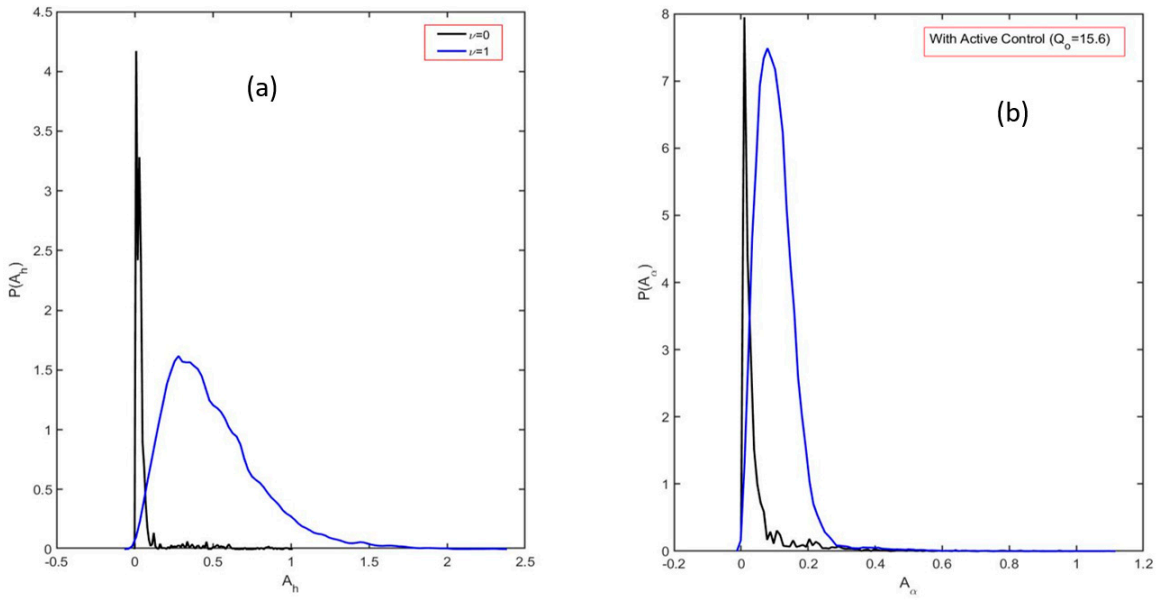

Figure 32. Probability density functions for aeroelastic displacements (closed-loop, $\nu = 1$). (**a**) Comparison of controlled bending (h) pdfs (un-forced & with random excitation). (**b**) Comparison of controlled pitch (α) pdfs (un-forced & with random excitation). Random excitation under active control causes diffusion and displacement from equilibrium positions.

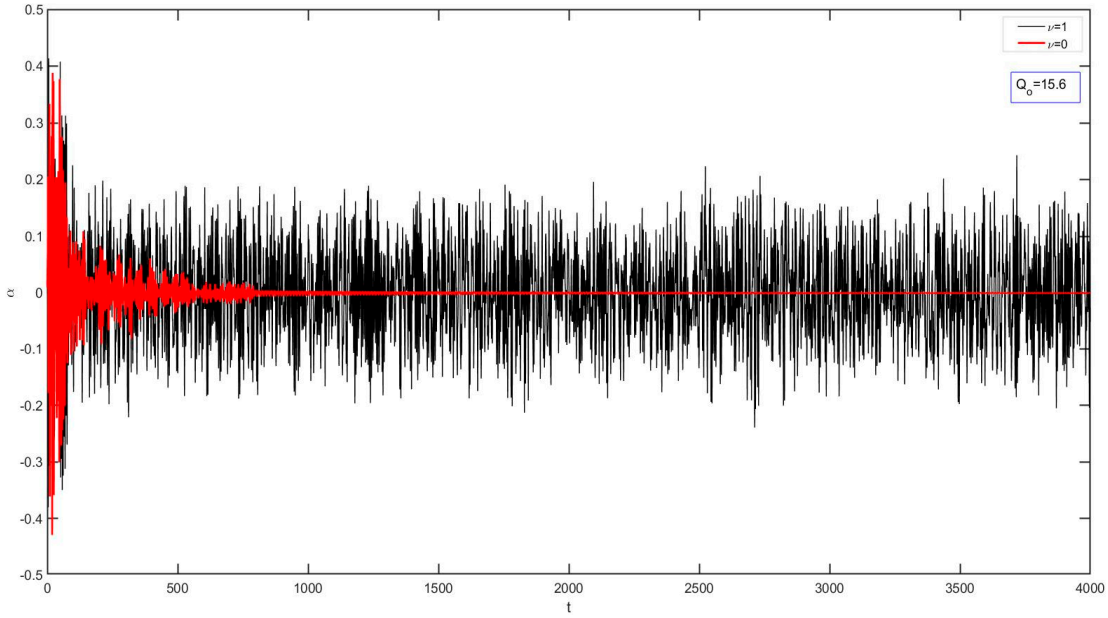

Figure 33. Effect of noise on torsional displacement with active control.

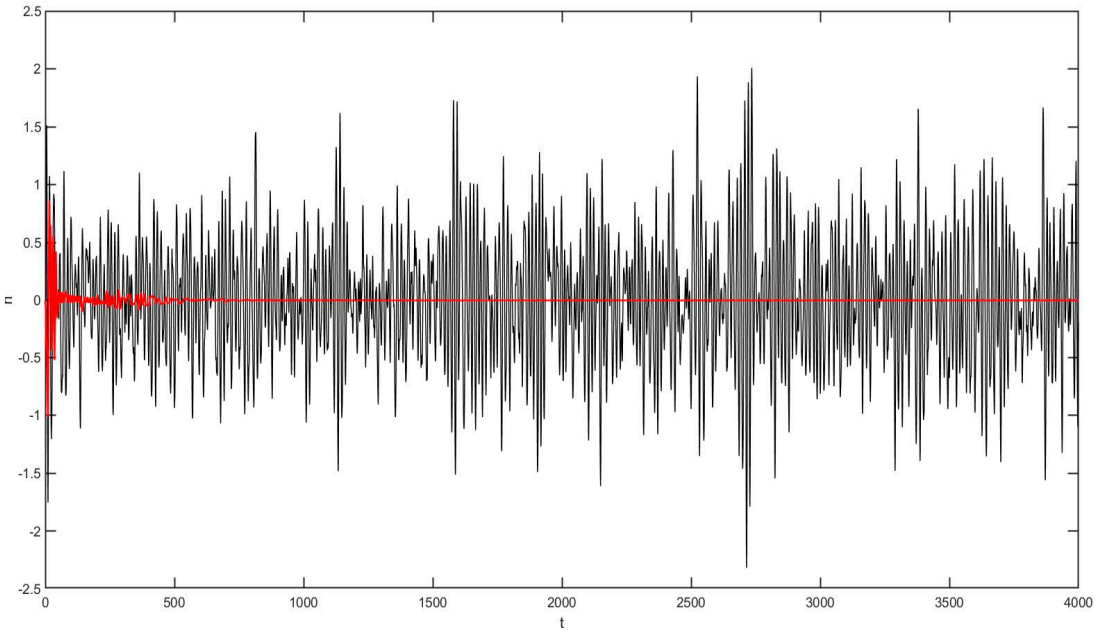

Figure 34. Effect of noise on bending displacement with active control.

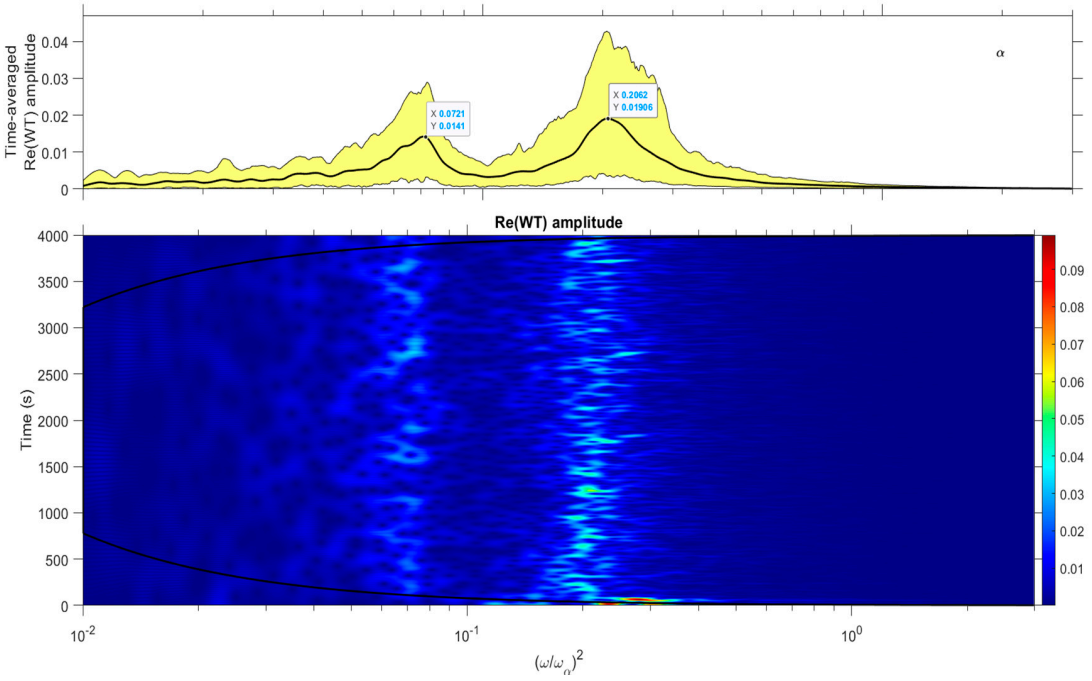

Figure 35. Time–frequency analysis (α, closed-loop, $\nu = 1$).

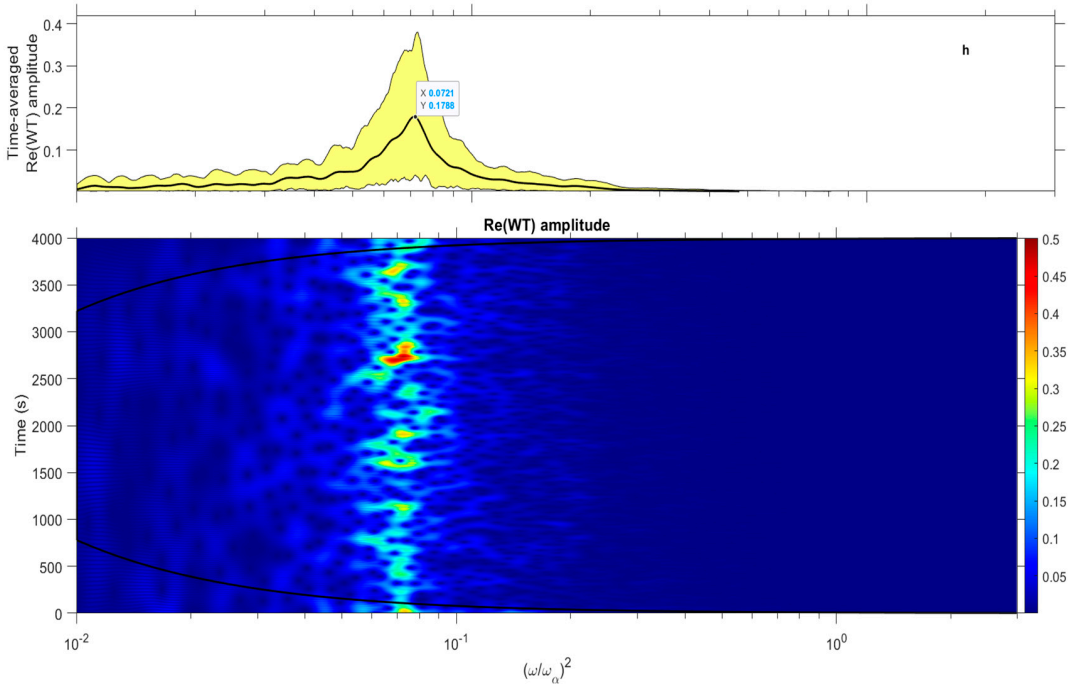

Figure 36. Time–frequency analysis (h, closed-loop, $\nu = 1$).

For Case III, we have seen that excitation by noise alone on the uncontrolled or open-loop system suppresses the phase-coherent chaotic response, which is beneficial to the wing structure. When the closed-loop system is subjected to excitation by noise, the aeroelastic displacements become destabilized. It is possible to mitigate this sensitivity to noise/turbulence by applying an adaptive filter to feedback signals before they are passed to the control scheme.

5. Conclusions

In this paper, the chaotic motions of a two-dimensional self-excited airfoil with a cubic nonlinear stiffness and linear viscous damping are controlled using closed-loop harmonic parametric excitation. Closed-loop harmonic parametric excitation is a linear combination of harmonic terms (or a single term) and is multiplied by the airspeed parameter Q_0. The torsional and bending displacements and their respective velocities (four states) are used in the arguments of the harmonic terms; the harmonic terms are bounded, and the feedback signals track the time-continuous changes in amplitude and frequency, this is called self-controlling feedback. Two configurations of the harmonic control perturbation signal are applied to the aeroelastic system. Case I: A cosine term whose mathematical argument is the product of the wing pitch rate and nondimensional time. The prescribed perturbation signal caused the nonlinear torsional dynamics to behave like a nonlinear energy sink in the chaotic regime for which the mechanism of vibration suppression is the resonance capture cascade. Below an airspeed parameter setting of 9, the closed-loop response is a limit cycle oscillation. It was also observed in the time–frequency domain that a resonance capture with energy absorption presents as an increase in spectral power in one degree of freedom while the other shows a significant decrease; this decrease in spectral power corresponds to a reduction in displacement amplitude in the linear degree of freedom. Case II: A linear combination of the first term from Case I and a sinusoidal term whose argument is the product of the bending displacement and the nondimensional time. The prescribed control perturbation signal for this case was found to induce an isolated resonance capture about the frequency ratio ~0.2951, indicated by a red arrow (see Figure 17). The perturbation signal provides broadband excitation that inhibits both the chaotic dynamics and the limit cycle oscillations. In addition, it was observed that the feedback can provide damping over a wide airspeed range. The mechanism of vibration suppression is the isolated resonance capture, which minimizes the energy exchange between the aeroelastic displacements. The control perturbation signal for this case is more appropriate for practical application primarily because it can suppress both the chaotic dynamics. The control approach can be improved by the application of force-limiting criteria in order to minimize the startup transients when the control is engaged at $t = 0$. Case III: The effect of simulated aerodynamic turbulence (Gaussian noise) on the open- and closed-loop nonlinear aeroelastic system was briefly examined. When the open-loop system is subjected to random excitation, the response is favorable in that the phase-coherent chaotic regime is suppressed, which is beneficial to the structure. When the closed-loop system is subjected to random excitation, the aeroelastic response is one of random limit cycle oscillations and is shifted to nonzero equilibrium positions. This can be mitigated by applying an adaptive filter in the feedback path to remove the turbulence-based noise from the raw signals before entry to the control scheme.

The contributions of this work can be summarized as follows:

1. It was identified that the harmonic signal, $\cos(\dot{\alpha}t)$, causes the nonlinear torsional degree of freedom to behave like a nonlinear energy sink.
2. Under closed-loop harmonic parametric excitation, it was identified that the mechanisms of vibration suppression are the *resonance capture cascade* and the *isolated resonance capture*. The mechanisms were identified using nonstationary signal processing methods.
3. It was successfully demonstrated that harmonic time-continuous control (via parametric excitation) can fully suppress the post-flutter dynamics of the aeroelastic system.
4. In addition to the above, it is now understood that random excitation with increasing intensity can suppress the phase coherence of the uncontrolled aeroelastic system. This particular configuration of control law, when employed, requires some type of adaptive filter to address flight and maneuver-induced turbulence.

6. Future Research

In general, the flutter control problem is frequency-based and sensitive to changes in operating condition and aircraft wing configuration; thus, it would be interesting to study the application of an adaptive control algorithm that can perform system identification and disturbance rejection simultaneously. One such algorithm is the ARMARKOV disturbance rejection algorithm.

The ARMARKOV disturbance rejection algorithm was successfully applied in active flow control experiments performed by Tian et al. [27]. The algorithm was first introduced by Venugopal and Bernstein (active noise control experiments) [28] and further developed by Sane et al. [29]. The algorithm uses a linear model that is identified simultaneously using the recursive ARMARKOV/Toeplitz system identification algorithm. The use of a linear model does not pose any serious limitations in its application to a nonlinear aeroelastic system provided the model is sufficiently accurate and is particularly appropriate for a dynamical system whose operating conditions (i.e., speed, altitude, aerodynamic turbulence, and gusts) can change rapidly. The algorithm has two parts: System identification and control. The system identification block develops a system model between the actuator voltage signals and the selected unsteady aeroelastic signal, while the control algorithm seeks to minimize the performance signal. The performance signal could be one of the aeroelastic states from the airfoil model given in this paper or an accelerometer signal that could come from a wind tunnel rig or from an aircraft. A block diagram of the algorithm is shown in Figure 37.

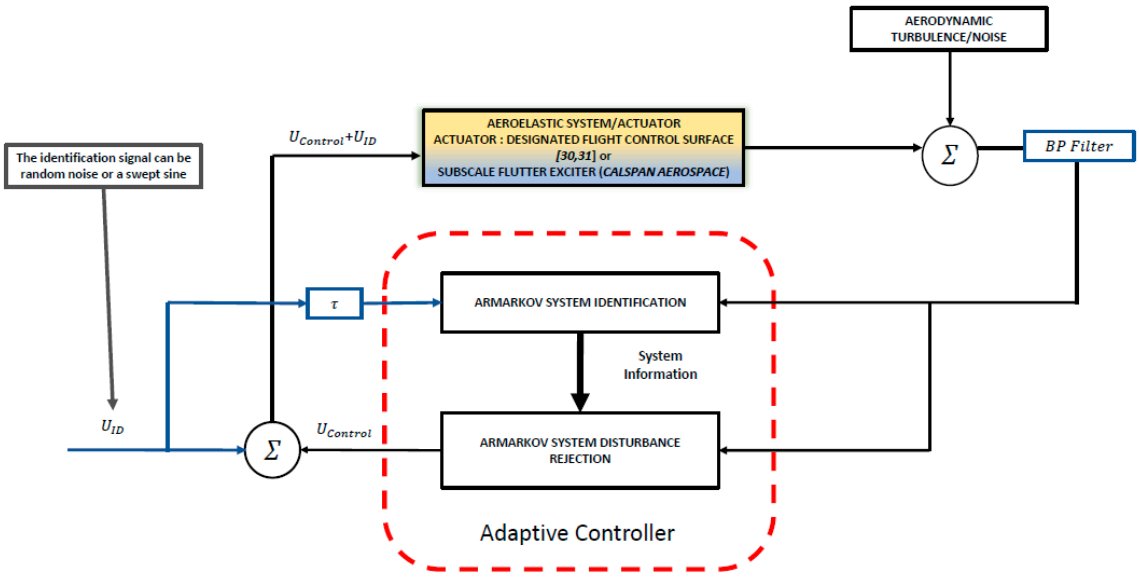

Figure 37. Schematic for adaptive system identification and disturbance rejection.

Both the identification and control signals form an effective control input into the nonlinear aeroelastic system, and the output signal is measured by the transducers and fed back to the adaptive control algorithm. The *identification algorithm* uses the input and output signals to develop a real-time linear model and provides the information needed by the disturbance rejection algorithm. The *disturbance rejection algorithm* uses the model and the measured performance signal (an accelerometer signal for load limiting [30], for example) to tune the controller. The resulting control signal is multi-harmonic and time-varying and can be implemented experimentally by using a subscale flutter exciter/function generator or designated flutter flight control surfaces like those found on the B-52 CCV [30,31] (see Figure 37). In the context of this current paper and the work presented by Ramesh and Narayanan [2], mechanizing the perturbation of the airspeed parameter may prove difficult. As such, this is a viable alternative for future research (simulation, wind tunnel testing, and flight test) and may provide an equivalent control solution (that accounts for aerodynamic turbulence and other

disturbances) to the closed-loop parametric excitation presented in the current work and by Ramesh and Narayanan.

Funding: This research has received no external funding

Conflicts of Interest: The authors declare no conflict of interest

References

1. Zhao, L.C.; Yang, Z.C. Chaotic motions of an airfoil with nonlinear stiffness in incompressible flow. *J. Sound Vib.* **1990**, *138*, 245–254. [CrossRef]
2. Ramesh, M.; Narayanan, S. Controlling chaotic motions in a two-dimensional airfoil using time-delayed feedback. *J. Sound Vib.* **2001**, *239*, 1037–1049. [CrossRef]
3. Tondl, A. To the Problem of Self-Excited Vibration Suppression. *Eng. Mech.* **2008**, *15*, 297–307. Available online: http://www.im.fme.vutbr.cz/pdf/15_4_297.pdf (accessed on 21 April 2020).
4. Dohnal, F.; Tondal, A. Suppressing Flutter Vibrations by Parametric Inertia Excitation. *ASME J. Appl. Mech.* **2009**, *76*, 1–7. [CrossRef]
5. Tondl, A.; Ecker, H. On the problem of self-excited vibration quenching by means of parametric excitation. *Arch. Appl. Mech.* **2003**, *72*, 923–932. [CrossRef]
6. Dohnal, F.; Ecker, H.; Springer, H. Enhanced damping of a cantilever beam by axial parametric excitation. *Arch. Appl. Mech.* **2008**, *78*, 935–947. [CrossRef]
7. Chin, C.; Nayfeh, A.H.; Mook, D.T. The response of a nonlinear system with a nonsemisimple one-to-one resonance to a combination parametric resonance. *Int. J. Bifurc. Chaos* **1995**, *5*, 971–982. [CrossRef]
8. Poirel, D.C.; Price, S.J. Post-instability behavior of a structurally nonlinear airfoil in longitudinal turbulence. *J. Aircr.* **1997**, *34*, 619–626. [CrossRef]
9. Ibrahim, R.A.; Castravete, S.C. Flutter suppression of a plate-like wing via parametric excitation. *Nonlinear Dyn.* **2006**, *46*, 387–426. [CrossRef]
10. Harold, T. Performance Characterization and Control of a Smart Spring Device for Indirect-Active Vibration Suppression. Master's Thesis, Carleton University, Ottawa, ON, Canada, 2004.
11. Cunefare, K.A.; De Rosa, S.; Sadegh, N.; Larson, G. State-Switched absorber for semi-active structural control. *J. Intell. Mater. Syst. Struct.* **2000**, *11*, 300–310. [CrossRef]
12. Wickramasinghe, V.; Chen, Y.; Zimcik, D. Experimental evaluation of the smart spring impedance control approach for adaptive vibration suppression. *J. Intell. Mater. Syst. Struct.* **2008**, *19*, 171–179. [CrossRef]
13. Yong, C.; Zimcik, D.G.; Wickramasinghe, V.K.; Nitzsche, F. Development of the smart spring for active vibration control of helicopter blades. *J. Intell. Mater. Syst. Struct.* **2004**, *15*, 37–47. [CrossRef]
14. Athalye, A.M. Notch Filter Feedback Control of a Chaotic System. Ph.D. Thesis, Washington State University at Pullman, Pullman, WA, USA, 1993.
15. Ahlborn, A.; Parlitz, U. Chaos control using notch filter feedback. *Phys. Rev. Lett.* **2006**, *96*, 034102. [CrossRef] [PubMed]
16. Pyragas, K. Continuous control of chaos by self-controlling feedback. *Phys. Lett. A* **1992**, *170*, 421–428. [CrossRef]
17. Poulimenos, A.G.; Fassois, S.D. Parametric time-domain methods for non-stationary random vibration modelling and analysis—A critical survey and comparison. *Mech. Syst. Signal Process.* **2006**, *20*, 763–816. [CrossRef]
18. Vakakis, A.F.; McFarland, D.M.; Bergman, L.; Manevitch, L.I.; Gendelman, O. Isolated resonance captures and resonance capture cascades leading to single-or multi-mode passive energy pumping in damped coupled oscillators. *J. Vib. Acoust.* **2004**, *126*, 235–244. [CrossRef]
19. Lee, Y.S.; Vakakis, A.F.; Bergman, L.A.; McFarland, D.M.; Kerschen, G.; Nucera, F.; Tsakirtzis, S.; Panagopoulos, P.N. Passive non-linear targeted energy transfer and its applications to vibration absorption: A review. *Proc. Inst. Mech. Eng. Part K J. Multi-Body Dyn.* **2008**, *222*, 77–134. [CrossRef]
20. Dekemele, K.; De Keyser, R.; Loccufier, M. Performance measures for targeted energy transfer and resonance capture cascading in nonlinear energy sinks. *Nonlinear Dyn.* **2018**, *93*, 259–284. [CrossRef]
21. Poirel, D.C.M. Random Dynamics of a Structurally Nonlinear Airfoil in Turbulent Flow. Ph.D. Thesis, McGill University, Montreal, QC, Canada, 2001.

22. Poirel, D.; Landry, N. DND Flutter Clearance Methodology-CF-18/480 USG EFT Category II Experience. In Proceedings of the CASI 40th Annual Conference, Toronto, ON, Canada, 5 May 1993.
23. Xu, Y.; Liu, Q.; Guo, G.; Xu, C.; Liu, D. Dynamical responses of airfoil models with harmonic excitation under uncertain disturbance. *Nonlinear Dyn.* **2017**, *89*, 1579–1590. [CrossRef]
24. Liu, Q.; Xu, Y.; Xu, C.; Kurths, J. The sliding mode control for an airfoil system driven by harmonic and colored Gaussian noise excitations. *Appl. Math. Model.* **2018**, *64*, 249–264. [CrossRef]
25. Liu, Q.; Xu, Y.; Kurths, J. Bistability and stochastic jumps in an airfoil system with viscoelastic material property and random fluctuations. *Commun. Nonlinear Sci. Numer. Simul.* **2020**, *84*, 105184. [CrossRef]
26. Ditzinger, T.; Ning, C.Z.; Hu, G. Resonancelike responses of autonomous nonlinear systems to white noise. *Phys. Rev. E* **1994**, *50*, 3508. [CrossRef] [PubMed]
27. Tian, Y.; Song, Q.; Cattafesta, L. Adaptive feedback control of flow separation. In Proceedings of the 3rd AIAA Flow Control Conference, San Francisco, CA, USA, 5–8 June 2006; p. 3016.
28. Venugopal, R.; Bernstein, D.S. Adaptive disturbance rejection using ARMARKOV/Toeplitz models. *IEEE Trans. Control. Syst. Technol.* **2000**, *8*, 257. [CrossRef]
29. Sane, H.S.; Venugopal, R.; Bernstein, D.S. Disturbance rejection using self-tuning ARMARKOV adaptive control with simultaneous identification. *IEEE Trans. Control. Syst. Technol.* **2001**, *9*, 101–106. [CrossRef]
30. Arnold, J.I.; Murphy, F.B. B-52 control configured vehicles: Flight test results. *Adv. Control Technol. Potential Future Transp. Aircr. NASA TM X-3409.* **1976**, *1*, 75–89.
31. Roger, K.L.; Hodges, G.E.; Felt, L. Active flutter suppression-a flight test demonstration. *J. Aircr.* **1975**, *12*, 551–556. [CrossRef]